



UNIVERSITÀ DEGLI STUDI DI TRIESTE

SEDE AMMINISTRATIVA DEL DOTTORATO DI RICERCA

XXII CICLO  
DEL DOTTORATO DI RICERCA IN  
NANOTECNOLOGIE

**Oxidation of supported PtRh particles:  
size and morphology effects**

(SSD FIS/03 – Fisica della Materia)

DOTTORANDO

**Matteo Maria Dalmiglio**

DIRETTORE DELLA SCUOLA

Chiar.mo Prof. Maurizio Fermeglia

(Università degli Studi di Trieste)

RELATORE

Dr. Luca Gregoratti

(Sincrotrone Trieste S.C.p.A.)

ANNO ACCADEMICO 2008 - 2009



*Volentieri*

# Abstract

The chemical transformations of supported PtRh particles ranging in size from a few micrometers to a few nanometres, and nanocrystalline films have been studied under identical oxidizing conditions by means of different chemical and structural characterization techniques; in particular the main technique used has been the scanning photoemission spectromicroscopy (SPEM) available at the EscaMicroscopy beamline of the Elettra Synchrotron Light Source. This novel experimental technique allows sample's chemical mapping with a spatial resolution of 100nm and the acquisition of photoemission spectra on regions with the same dimension, and allow us to determine the chemical state of single micro-particles. In particular we studied PtRh cluster deposited by PLD (pulsed laser deposition) on a tungsten single crystal (W(110)) covered by a thin magnesium oxide film (MgO).

Significant variations of the Pt and Rh atoms reactivity have been revealed by comparing the oxidation states of particles with different dimensions and, for the micron-scale particles, also within the same island.

It was demonstrated that a selected oxidation occurs: rhodium atoms undergo stronger and faster oxidation than platinum ones. Furthermore, the oxidation process is composed by many intermediate steps, in which metastable oxides are formed. Very small cluster's oxidation (<10nm diameter) is significantly faster than the bigger one (>100nm). Some morphological and structural clusters' modifications after long oxidation treatments were also investigated using a high resolution SEM (<2nm lateral resolution).

Other measurements have been performed by using a Low Energy Electron Microscope (LEEM) that combines a high spatial resolution (<5nm) to a high sensitivity to surface structural modifications. In particular the behaviour of the clusters' polycrystalline structure has been studied during oxidation-reduction treatments. It has been shown that the clusters' surface is polycrystalline and that each nano crystals have different crystallographic orientation. After oxidation each nano-crystal undergoes a different oxidation rate. The diffraction pattern revealed that after a long oxidation the long range order of the particles' surface is completely lost.

A characterization of the reactivity of the PtRh particles towards oxidation after an “ageing” process based on the repetition of many redox cycles has revealed a change in the stability of the oxides.

Other experiments have been realized with SEM and EDX for studying the clusters’ morphology at different annealing temperatures. The results have shown structural, chemical and morphology changes.

# Sommario

In questa tesi tramite diverse tecniche di caratterizzazione chimica e strutturale sono state studiate le trasformazioni chimiche di particelle di platino-rodio (PtRh), di dimensioni variabili tra pochi nanometri e pochi micron, e di film nano cristallini, durante processi di ossidazione. In particolare la tecnica di analisi principale è stata quella della spettroscopia a scansione in fotoemissione (SPEM) che è disponibile sulla beamline EscaMicroscopy nel laboratorio di luce di sincrotrone Elettra. Questa tecnica sperimentale permette di mappare la superficie di un campione con una risoluzione spaziale di 100nm e di acquisire spettri di fotoemissione su regioni con le stesse dimensioni, permettendo di determinare lo stato chimico di singole micro particelle.

In particolare abbiamo studiato le proprietà di ossidazione di cluster di PtRh depositati mediante PLD (pulsed laser deposition) su un cristallo singolo di tungsteno (W(110)) ricoperto da un sottile film di ossido di magnesio (MgO).

Comparando gli stati di ossidazione di particelle con differenti dimensioni si sono rilevate significative variazioni di reattività per gli atomi di Pt e di Rh e, per le particelle di dimensioni micrometriche, si è visto che tali variazioni avvengono anche all'interno della stessa particella.

Si è dimostrato che avviene un'ossidazione selettiva: gli atomi di rodio si ossidano maggiormente e più velocemente di quelli di platino. Inoltre il processo di ossidazione è composto da molti passaggi intermedi in cui si formano ossidi metastabili. L'ossidazione di cluster più piccoli (con un diametro minore di 10nm) è significativamente più veloce di quelli più grandi (>100nm).

Tramite l'uso di un microscopio elettronico a scansione (SEM) ad alta risoluzione (risoluzione laterale inferiore ai 2 nm) sono state studiate alcune modifiche morfologiche e strutturali dopo lunghi trattamenti di ossidazione.

Altre misure sono state effettuate sulla beamline Nanospectroscopy usando un *Low Energy Electron Microscope* (LEEM) che unisce un'alta risoluzione spaziale (<5nm) con un'alta sensibilità alle modifiche strutturali di superficie. Si è evidenziato come i cluster presentino una superficie policristallina dove l'orientazione dei vari nanocristalli è diversa da zona a zona e come i vari cristalli vadano incontro a diversi stati di

ossidazione. In particolare analizzando i pattern di diffrazione abbiamo osservato che dopo una lunga ossidazione si perdono completamente le informazioni sulla struttura atomica ordinata della superficie presente invece sulle particelle ridotte.

È stata effettuata una caratterizzazione della reattività di particelle di PtRh dopo un processo di invecchiamento basato sulla ripetizione di diversi cicli di ossido-riduzione che ha rivelato un cambiamento nella stabilità degli ossidi formati: a parità di ossidazione le particelle “invecchiate” si riducono molto più facilmente.

Sono stati effettuati altri esperimenti atti a caratterizzare la morfologia e il comportamento ad alte temperature dei cluster mediante l’ausilio di un microscopio SEM e di un sistema EDX (*Energy dispersive X-ray spectroscopy*) ad esso equipaggiato. Si è visto come prolungati trattamenti termici modificano la chimica, la struttura e la morfologia superficiale delle diverse facce che costituiscono i cluster.

---

## Contents

<b>1. Introduction</b>	<b>1</b>
<b>2. Experimental techniques used for the preparation and characterization of the samples</b>	<b>8</b>
2.1. Photoemission and Synchrotron radiation .....	8
2.1.1. Principles of Photoemission.....	8
2.1.2. Synchrotron radiation.....	11
2.1.3. The Elettra Synchrotron Light Source .....	13
2.2. The Scanning PhotoElectron Microscope (SPEM).....	14
2.2.1. The SPEM Microscope at the ESCA microscopy Beamline at Elettra	16
2.2.2. Hemispherical Electron Analyzer and Detectors .....	17
2.2.3. Multichannel Detection: Spectra and Detectors.....	19
2.3. Low Energy Electron Diffraction (LEED) .....	21
2.4. Low Energy Electron Microscope (LEEM).....	23
2.4.1. LEEM setup .....	23
2.4.2. LEEM methods .....	24
2.5. Pulsed Laser Deposition (PLD) technique.....	26
2.6. Other Techniques of Surface Science used: AES, SEM and EDX.....	29
2.7. Micro Wave Plasma source .....	32
<b>3. Sample preparation and characterization</b>	<b>36</b>
<b>4. Oxidation states of single particles monitored by SPEM</b>	<b>44</b>
4.1. Working conditions.....	44
4.2. Results .....	44
<b>5. Structural changes evidenced by LEEM and <math>\mu</math>-LEED</b>	<b>56</b>

---

<b>6. Other results</b>	<b>63</b>
6.1. Bulk-surface stoichiometry .....	63
6.1.1. PE and EDX measurements .....	63
6.2. Morphological changes by annealing .....	65
6.2.1. Evolution of the morphology analyzed by SEM.....	65
6.2.2. Stoichiometry after annealing .....	70
6.3. Photon Beam Induced Reduction.....	71
6.3.1. Ageing effects after redox cycles.....	71
6.4. Partial coverage of a single multi-wall carbon nanotube.....	73
6.4.1. Carbon Nanotubes (CNTs).....	73
6.4.2. Experimental setups for the partial coverage of a single MWCN .....	75
6.4.3. Deposition of PtRh clusters on MWCNTs.....	77
<b>7. Conclusions .....</b>	<b>80</b>

# Chapter 1

## Introduction

A chemical reaction is a process in which one or more species, the reactants, undergo a transformation to become new species called products. A special class of chemical reactions is formed by the *activated processes*, for which the chemical transformation requires a supplied energy to start.

This energy is supplied by *catalysts*: a catalyst is a substance that transforms reactants into products, through an uninterrupted repeated cycle of elementary steps in which the catalyst participates while being regenerated in its original form at the end of each cycle. The catalyst's activity represents the number of revolutions of the cycle per unit time (turnover rate).

This is possible because a catalyst forms bonds with reactants, thus allowing these to react and give rise to products while leaving the catalyst in its original form. In this way it is possible to offer a more complex but at the same time energetically favourable and more rapid path to final products, reducing the activation energy of the process, hence resulting in an increased reaction rate. The catalyst does not modify the thermodynamics of a system but acts on its kinetics.

Catalysis can be classified into three main classes. In bio-catalysis, reactions involve biological species and enzymes play the role of catalysts. In homogeneous catalysis the reactants and the catalyst are in the same physical state. In heterogeneous catalysis, catalysts are in solid state and favour the reactions of species in liquid or gas phase. The experiments reported in this thesis deal with the latter class.

The importance of heterogeneous catalysis in chemical and related industries is well known. Approximately 90% of all chemical industry products are made using catalytic processes [1, 2, 3]. Catalysts play also a crucial role in the abatement of environmental

pollution in automotive and industrial exhausts. They are essential in the development of efficient fuel cells, where hydrogen has become a potential idea fuel for the future.

Their importance therefore justifies the intense ongoing research efforts in this field and in finding more stringent requirements for less expensive and more efficient catalysts.

Despite its importance in so many different and fundamental processes, explanations of many of the phenomena involved in catalysis are still lacking, thus providing significant motivation for fundamental research in this field. This is due to the considerable chemical and structural complexity, mainly in the size and the structure, of real catalysts which are usually powders, composed of transition metal (TM) nanoparticles supported by oxide layers. These nanoparticles expose different facets, as well as defects like steps, kinks or missing atoms, which are considered to be the most reactive sites.

On real catalysts there are different active sites and their properties arise from the interplay of many different effects: the size of active particles, the interaction between particles and support, the surface morphology of active materials. Thus, understanding the relation between surface heterogeneity, morphology, and chemical reactivity will provide us with key insight into what researchers in catalysis call “selectivity”[4] i.e. the amount of a desired product obtained per amount of consumed reactant.

When characterizing a particular measurable quantity (for example, the chemical reactivity of the catalyst) it is not possible to disentangle the different contributions in a direct way: in this correlation of causes lies the “complexity” of real catalysts. One possible way to overcome some of this complexity is to study so-called model systems. Model systems are physical systems that are simpler to understand than real catalysts, but that can be manipulated by experimentalists in order to determine which of their features is responsible for their chemical properties.

The fabrication of model catalysts in the context of this work requires the growth of flat, thin, crystalline, metal oxide films on a metal single crystal surface. Metallic or oxidic nanoparticles are deposited subsequently. A typical model is shown in Fig 1.1: a metallic single crystal is used as a substrate for a thin oxide film, over which nanoparticles are deposited as the active phase.

The presence of a metal oxide film is due to the fact that in a catalyst, a catalytically active component, such as a transition metal, is dispersed over a suitable support material —usually an oxide like alumina or silica. In the first place, this is done in order to achieve the highest possible surface area of the active phase.

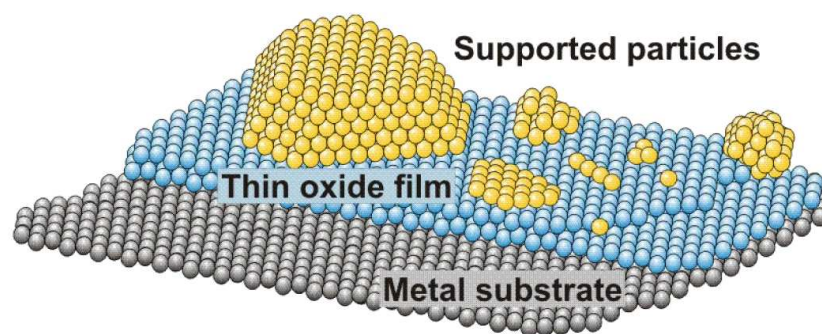


*Figure 1.1:* Schematic of a typical surface science compatible model catalyst. Within this work, the supported particles are PtRh clusters produced by PLD

There is still only very limited fundamental knowledge about the relationship and the interplay between structure, adsorption behaviour, and chemical or catalytic activity of small deposited metal aggregates. It is a well known fact and the basis of many of today's technological applications that the catalytic properties of alloys are often superior to those of pure metals and they have found broad applications in many industrial processes of synthesis and exhaust gas converters [5]

When exploring the behavior of the alloys it has been shown that the individual metal atoms generally maintain their properties, and the ligand effects due to alloying usually result in modifications that should improve the catalyst efficiency [6, 7]. The ligand effect represents the modification of the adsorptive properties of a given site via electronic effects by the neighbours (ligands) of an atom that a given adsorbate binds to; it is also related to the notion of chemical bonding and plays an important role in the chemistry of molecules [7]. In order to identify the proper alloys that will show superior catalytic behaviour for specific reactions it is necessary to understand the electronic structure [8].

A textbook example in this respect is the PtRh alloy, one of the most efficient automobile gas converter catalysts, and recently also considered as promising electrocatalyst for use in fuel cells [9].

hydrogen 1 H 1.0079																	helium 2 He 4.0026						
lithium 3 Li 6.941	beryllium 4 Be 9.0122																	boron 5 B 10.811	carbon 6 C 12.011	nitrogen 7 N 14.007	oxygen 8 O 15.999	fluorine 9 F 18.998	neon 10 Ne 20.180
sodium 11 Na 22.990	magnesium 12 Mg 24.305																	aluminum 13 Al 26.982	silicon 14 Si 28.086	phosphorus 15 P 30.974	sulfur 16 S 32.065	chlorine 17 Cl 35.453	argon 18 Ar 39.948
potassium 19 K 39.098	calcium 20 Ca 40.078	scandium 21 Sc 44.956	titanium 22 Ti 47.867	vanadium 23 V 50.942	chromium 24 Cr 51.996	manganese 25 Mn 54.938	iron 26 Fe 55.845	cobalt 27 Co 58.933	nickel 28 Ni 58.693	copper 29 Cu 63.546	zinc 30 Zn 65.38	gallium 31 Ga 69.723	germanium 32 Ge 72.61	arsenic 33 As 74.922	selecnium 34 Se 78.96	bromine 35 Br 79.904	krypton 36 Kr 83.80						
rubidium 37 Rb 85.468	strontium 38 Sr 87.62	yttrium 39 Y 88.906	zirconium 40 Zr 91.224	niobium 41 Nb 92.906	molybdenum 42 Mo 95.94	technetium 43 Tc [98]	ruthenium 44 Ru 101.07	rhodium 45 Rh 101.07	palladium 46 Pd 106.36	silver 47 Ag 107.87	cadmium 48 Cd 112.41	indium 49 In 114.82	tin 50 Sn 118.71	antimony 51 Sb 121.76	tellurium 52 Te 127.60	iodine 53 I 126.90	xenon 54 Xe 131.29						
cesium 55 Cs 132.91	barium 56 Ba 137.33	lanthanum 57 La 138.91	hafnium 71 Hf 178.49	tantalum 72 Ta 180.95	tungsten 73 W 183.84	rhenium 74 Re 186.21	osmium 75 Os 190.23	iridium 76 Ir 192.22	platinum 77 Pt 195.08	gold 78 Au 196.97	mercury 79 Hg 200.59	thallium 80 Tl 204.38	lead 81 Pb 207.2	bismuth 82 Bi 208.98	polonium 83 Po [209]	astatine 84 At [210]	radon 85 Rn [222]						
francium 87 Fr [223]	radium 88 Ra [226]	* * * * *																					
		actinium 89 Ac [227]	thorium 90 Th 232.04	protactinium 91 Pa 231.04	uranium 92 U 238.03	neptunium 93 Np [237]	plutonium 94 Pu [244]	americium 95 Am [243]	curium 96 Cm [247]	berkelium 97 Bk [247]	californium 98 Cf [251]	einsteinium 99 Es [252]	fermium 100 Fm [257]	mendelevium 101 Md [258]	nobelium 102 No [259]								

* Lanthanide series													
lanthanum 57 La 138.91	cerium 58 Ce 140.12	praseodymium 59 Pr 140.91	neodymium 60 Nd 144.24	promethium 61 Pm [145]	samarium 62 Sm 150.36	europium 63 Eu 151.96	gadolinium 64 Gd 157.25	terbium 65 Tb 158.93	dysprosium 66 Dy 162.50	holmium 67 Ho 164.93	erbium 68 Er 167.26	thulium 69 Tm 168.93	ytterbium 70 Yb 173.04
** Actinide series													
actinium 89 Ac [227]	thorium 90 Th 232.04	protactinium 91 Pa 231.04	uranium 92 U 238.03	neptunium 93 Np [237]	plutonium 94 Pu [244]	americium 95 Am [243]	curium 96 Cm [247]	berkelium 97 Bk [247]	californium 98 Cf [251]	einsteinium 99 Es [252]	fermium 100 Fm [257]	mendelevium 101 Md [258]	nobelium 102 No [259]

Figure 1.2: Elements periodic table. Pt and Rh are highlighted.

In this alloy the individual Pt metal is the most active in CO oxidation, whereas Rh adds the needed high activity for NO reduction to N<sub>2</sub>. Despite the well known efficiency of this alloy at high temperature, e.g. steady-state automotive catalytic converters which operate above 700°C, still its behaviour at lower temperatures, present for instance in the cold-start emissions for automobiles or in fuel cells, has to be deeply delved [10].

Surface science compatible model catalysis suffers from two drawbacks: the pressure gap, and the materials gap. The term “pressure gap” refers to the fact that the pressure regime under which surface science experiments are carried out, differs from the industrial application by several orders of magnitude. The issue that the models consist of thin films, which are novel materials specifically created for these studies, and that their structural and electronic properties might not be comparable to the corresponding industrial catalyst, is summarized as the “material gap”.

The basic knowledge for the catalytic properties of the individual metals in the PtRh alloy in oxidation/reduction reaction is provided by studies with model systems following a bottom-up approach aimed at bridging this “material gap” between model and real supported catalysts.

These systems are with increasing complexity and include Pt and Rh single crystal, vicinal and highly defective surfaces, as well supported micro- and nano-particles. The studies of single crystal and vicinal and defective surface have already provided a

detailed picture of the oxygen-related adsorption, transient surface oxide and bulk oxide structures, including the strong effects of the surface morphology, in particular the presence of under-coordinated atoms at the vicinal and defective surfaces [11, 12]. Under oxidation conditions the structure of the initial metal plane can undergo drastic changes, e.g. oxide formation on Pt(110) can result in a disordered phase [13]. Bimetallic systems have an increased complexity, since they have another variable, the local organization of the two metals and the actual surface composition, which is strongly dependent on the gas environment and temperature. In the recent report it has been evidenced that due to the presence of different species there is a complex balance between the energetic terms which determine the catalytically active surface composition of PtRh bimetallic catalysts under oxidation-reduction reaction conditions [12].

The effect of surface structure and composition becomes less predictable with decreasing dimensionality, as evidenced by the studies of model supported metal particles of different size and shape [14, 15]. Even in such model systems the particles are not identical and due to geometric or electronic reasons they may behave as individual micro-reactors, differing with respect to their catalytic activity and/or selectivity. Recent in-situ X-ray photoelectron spectroscopy (XPS) studies comparing the CO oxidation on Rh nano-particles of different sizes showed increased oxide formation over smaller particles and correlated to that higher catalytic activity [16]. These findings, based on using a combination of microscopic and spectroscopic methods for exploring the local surface composition and structure, are concomitant with the size distribution in real catalyst particles, containing appreciable number of coordinatively unsaturated surface atoms, which can promote surface stress and elevated atomic mobility [17]. For the majority of catalyst particles, being in sub-10 nm range, quantum size and support interfacial effects can play important role as well. For the particular case of the PtRh bimetallic particles a large number of electron microscopy and x-ray diffraction studies have been focused on looking for correlations between their morphology, structure and catalytic activity in specific reactions, considering only the particles bulk composition determined by the preparation procedures [9, 18, 19]. Thermodynamic calculations and a limited number of XPS studies have indicated similar temperature and gas adsorption effects on the surface composition, as observed, for instance, with single crystal surfaces [19, 20]. Most of the studies of alloy particles with different Pt and Rh weight have reached the consensus

that before being exposed to reactive gases the outer shell is enriched with Pt [18], with exception of one case reporting Rh enrichment of the surface after exposure to hydrogen [21]. Similar dynamic response behaviour has recently been reported for bimetallic RhPd and PtPd nanoparticle catalysts, which undergo structural and chemical changes in response to reactive environments [8].

The present thesis work describes a synchrotron-radiation-based scanning photoelectron microscopy (SPEM) study of a system of supported bimetallic PtRh particles. In order to unravel the relative activity of the different PtRh particles under identical oxidizing-reducing reaction conditions and to look for correlations with the local surface composition evolved under the actual reaction conditions, a model system was prepared using Pt<sub>50</sub>Rh<sub>50</sub> target and the Pulsed Laser Deposition setup. Samples prepared with this procedure contain a great variety of particles with different size and shape. In this way it is possible to investigate the catalytic properties in function of the different size and of their complex morphology and structure.

Carbon nanotubes (CNT) are a fascinating material due to their unique properties and potential application as supporting material building block of modern nanodevices; moreover the metal–CNT interaction is a key point of the modern research since it plays a significant role in the integration of the next generation of nanodevices. [22]. For this reason carbon nanotubes could be considered as a novel support also for catalytic metal particles. In the last part of this thesis few preliminary results obtained from the deposition of PtRh clusters on multiwalled-CNT will be presented.

This thesis is organized as follows:

Chapter 2 gives a brief overview on the experimental technique used, with a particular attention to the Scanning PhotoElectron Microscopy (SPEM).

Chapter 3 is devoted to describe the sample preparation and characterization.

Chapter 4 deals with the oxidation of the PtRh particles monitored by SPEM, while chapter 5 is focused on the results showing the structural changes of these particles evidenced by LEEM and  $\mu$ -LEED.

Chapter 6 concerns with other results: photoemission and fluorescence measurements aimed at the definition of the particle bulk-surface stoichiometry, morphological changes induced by annealing, beam induced reduction of the particles and the deposition of PtRh clusters on multiwall carbon nanotubes.

---

**References**

- 1 Chorkendorff, J.; Niemantsverdriet, J.W.; Concepts of Modern Catalysis and Kinetics WILEY-VCH GmbH & Co. KgaA, **2003**.
- 2 European White Book on Fundamental Research in Materials Science, <http://www.mpg.de/english/illustrationsDocumentation/documentation/europWhiteBoo>
- 3 Bell, A.T. *Science*, **2003**, 299, 1688.
- 4 Boudart, M. In Perspectives in Catalysis; Thomas, J.M.; Zamaraev, K.I.; Eds.; Blackwell: Oxford, **1992**, p. 183.
- 5 Sinfelt, J.H. "Bimetallic Catalysts: Discoveries, Concepts and Applications....", Wiley: New York, , **1983**.
- 6 Somorjai, G. A. Surface Chemistry and Catalysis; Wiley: New York, **1994**
- 7 Gauthier, Y. et al, *Phys.Rev.Lett.* **2001**, 87, 36103
- 8 Jøhannesson, G.H.; Bligaard, T.; Ruban, A.V.; Skriver, H.L.; Jacobsen, K.W.; Nørskov, J.K. *Phys. Rev. Lett.* **2002**, 88, 255506
- 9 Park, K.-W.; Han, D.-S.; Sung, Y.-E. *J. of Power Sources* **2006**, 163, 82-86
- 10 Lyman, C.E.; Lakis, R.E.; Stenger Jr., H.G. *Ultramicroscopy* **1995**, 58, 25-34.
- 11 Wouda, P.T.; Schmid, M.; Hebenstreit, W.; Varga, P. *Surf. Sci.* **1997**, 388, 63-70
- 12 Baraldi, A.; Giacomello, D.; Rumiz, L.; Moretuzzo, M.; Lizzit, S.; Buatier De Mongeot, F.; Paolucci, G.; Kiskinova, M. *J. Am. Chem. Soc.* **2005**, 127, 5671-5674
- 13 Hendriksen, B.L.M.; Frenken, J.W.M. *Phys. Rev.Lett.* **2002**, 89, 046101
- 14 Dudin, P.; Barinov, A.; Gregoratti, L.; Scaini, D.; He, Y.B.; Over, H.; Kiskinova, M. *J. Phys. Chem. C* **2008**, 112, 9040–9044
- 15 Libuda, J.; Freund, H.-J. *Surf. Sci. Rep.* **2005**, 57, 157
- 16 Grass, E.; Y. Zhang, Y.; Butcher, D.R.; Park, J.Y.; Li, Y.; Bluhm, H.; Bratlie, K.M.; T. Zhang, T.; Somorjai, G.A. *Angew. Chemie Intern.* **2008**, 47, 8893
- 17 Ajayan, P.M.; Marks, L.D. *Phys. Rev. Lett.*, **1989**, 63, 279; Lai, S.L. et al. *Phys. Rev. Lett.* **1996**, 77, 99
- 18 Paál, Z.; Gyorffy, N.; Wootsch, A.; Tóth, L.; Bakos, I.; Szabó, S.; Wild, U.; Schlögl, R. *Z. J. of Catalysis* **2007**, 250, 254-263.
- 19 Dhepe, P.L.; Fukuoka, A.; Ichikawa, M. *Phys. Chem. Chem. Phys.* **2003**, 5, 5565.
- 20 Mezey, L.Z.; Hofer, W. *Surf. Sci.* **1998**, 402-404, 845-850
- 21 L. Zhu et al. *J. of Catalysis* **1997** 167, 408-411.
- 22 Bittencourt, C.; Feten, A.; Douhard, B.; Ghijsen, J.; Johnson, R.L.; Drue, W.; Pireaux, J.-J. *Chem. Phys.* **2006**, 328, 385-391.

# Chapter 2

## Experimental Techniques used for the preparation and characterization of the samples

### 2.1. Photoemission and Synchrotron radiation

Electron storage rings are now in their third generation. The fields of application for the radiation produced by synchrotrons are extremely wide and range from surface science to medical research. In addition, many conventional techniques have improved their performance and have expanded their field of application by using the synchrotron radiation. Among these, photoemission must certainly be included.

#### 2.1.1. Principles of Photoemission

The roots of X-ray Photoelectron Spectroscopy (XPS) can be traced back to the discovery of the photoelectric effect by Hertz, the description of its energetics by Einstein, and to the publication of XPS spectra from several metals by Robinson and Rawlinson [1, 2]. Siegbahn et al. [3] managed to develop XPS into a sensitive, high-resolution method for the determination of binding energies of electrons. Today, XPS is applied to a wide range of materials and provides information about their composition and, to a lesser extent, bonding and structure.

In an XPS experiment electrons are photoionized from the core levels by X-rays. The X-rays can be produced by conventional sources (Al and Mg anodes are the most common sources) or by synchrotron sources.

The cornerstone of XPS is the measurement of the kinetic energy  $E_{kin}$  of the outgoing electron. This energy is related to the electron binding energy  $E_b$  in this way:

$$E_{kin} = h\nu - E_b - \Phi_{sample} \quad (2.1)$$

Here  $h\nu$  is photon energy of the incident X-rays and  $\Phi_{sample}$  is the extra-energy needed to reach the vacuum level far away the atom;  $h\nu$  and  $\Phi_{sample}$  are known.

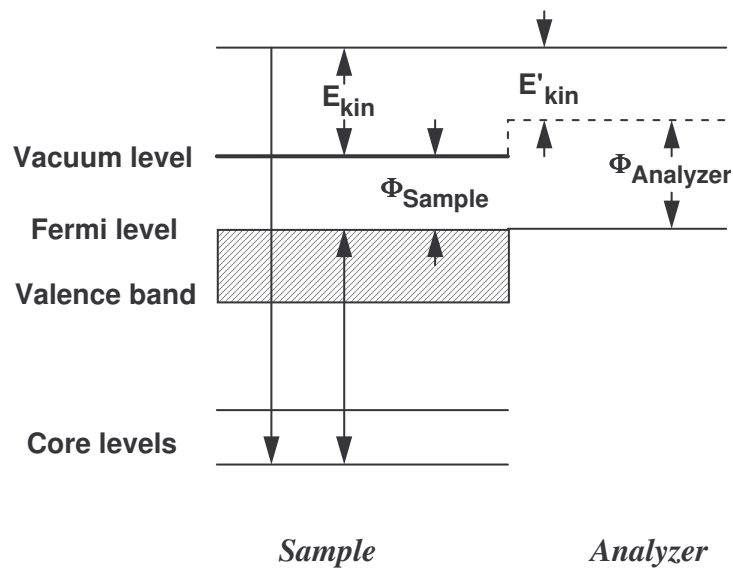


*Figure 2.1: Graphical description of equation (2.1)*

As shown in Fig.2.1 it must be noted that in order to be detected the photoelectron emitted with  $E_{kin}$  has to overcome the work function of the electron analyzer,  $\Phi_{analyzer}$  which is typically low, and then it will be detected with an energy  $E'_{kin}$ . Usually the position of the Fermi level is defined as the reference level ( $E_b=0$ ).

Contemporary XPS provides information about the environment of surface atoms [4]. Though core electrons are very localized and their wavefunctions are hardly affected by the surrounding, the binding energy of a core electron depends on the charge of the atom as well as on the background electrostatic potential in the core region. The matter is somewhat complicated by the dependence of the binding energy on the efficiency of

dielectric screening. These factors (background potential, charge and screening) are different on the surface than in the bulk. The differences are often called Surface Core Level Shifts (SCLS). The sign and the magnitude of the shift, which may range from few tenths of eV to a few eV, are signatures of the local environment of a surface atom. Screening enters into the description of the core level shifts because the electrons ejected from the solid leave a core hole [5, 6]. The energy of this hole depends on how efficiently its charge is screened by the electrons of the crystal, and reflects the energy of the core electron before it is ejected (initial state approximation) or rather the energy of the core hole (final state approximation). The answer depends on how efficiently the other electrons can screen the hole within the time needed for the photoemission process. If the surrounding electrons react extremely slowly, the ejected electron escapes as in the initial state picture. If the surrounding electrons react extremely fast, the ejected electron takes with it the whole screening energy and the final state picture with static screening of the hole is valid. Generally the photoelectron can take only a part of the screening energy. One should thus consider dynamical screening effects; the energy of the photoelectron is expected to be somewhere between the limits set by the initial state and final state approximations. In any case screening of the hole causes the photoelectron to appear at a higher kinetic energy, reducing its measured binding energy.

In the soft X-ray regime radiation can penetrate a few microns into condensed matter but because of the limited escape depth of the photoelectrons (a few nanometers at such energies), the intensity of the emitted photoelectrons is proportional to the number of illuminated atoms typically within one escape depth of the surface. This is the basis of a quantitative XPS analysis [7].

### **2.1.2. Synchrotron Radiation**

The line sources of X-rays used in conventional XPS are of course discrete, and for some type of experiments that represents a severe limitation. What is needed is a source of adequate intensity capable of being tuned continuously over the required energy range, and for this, a synchrotron radiation source is particularly suitable.

A synchrotron source exploits the fact that, when a charged body is accelerated it emits radiation, a process that is particularly efficient for an electron because of its small mass. Electrons are accelerated to relativistic velocities around an approximately

circular torus by pulsed electro-magnetic fields, and since they are forced into curved paths they emit light in a continuous spectrum. The intensity of the light  $I$  is described by the following expression:

$$I \propto \frac{T^4}{R^2} \quad (2.2)$$

where  $R$  is the radius of curvature of the path and  $T$  is the electron energy. In addition the emitted radiation is concentrated in a cone tangential to the electron orbit, with a small angular divergence. It is thus ideal for passage through a monochromator for energy selection. The universal characteristic curve for the shape of the radiation spectrum emitted by an electron moving in a curved orbit is shown in Fig. 2.2.

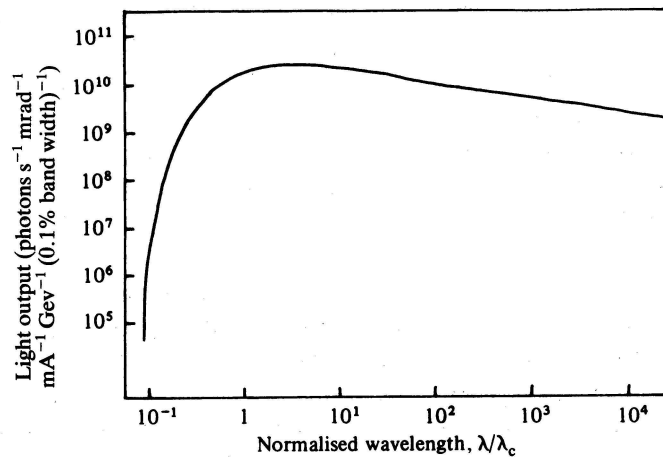


**Figure 2.2:** “Universal” spectral curve for synchrotron radiation. The emitted wavelength  $\lambda$  is normalized to  $\lambda_c$  which is characteristic of the synchrotron or storage ring.  $\lambda_c$  is also called the critical wavelength and characterizes the upper limit of the x-ray range produced by the ring.

The radiation flux can be increased by using special devices such as wigglers and undulators, which force the electrons to have locally a zigzag trajectory, and enhance the brilliance of the emitted radiation. They are typically used at 3<sup>rd</sup> generation synchrotron sources. A schematic view of an undulator section is shown in Fig. 2.3; the

letters  $N$  and  $S$  identify the poles of the magnetic field used to deviate the trajectory of the electrons.

Monochromator design and radiation and undulators physics are complex and specialized and this is not the appropriate place to discuss them in detail (a complete description of these devices can be found in Refs. 8 and 9).

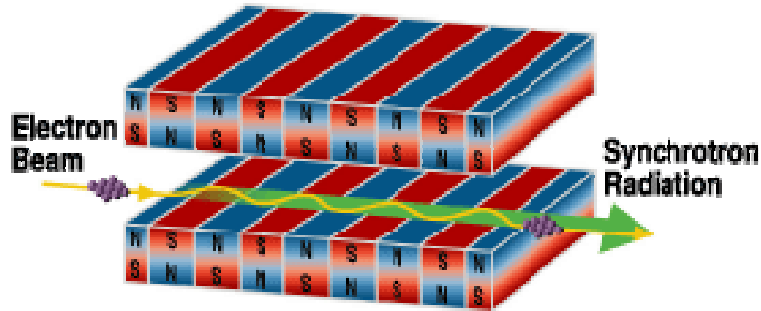


**Figure 2.3:** Schematic picture of an undulator (or wiggler). It consists of a periodic series of magnets, placed in a ring section where the electron path would otherwise be straight; because of its action, the electrons are forced to wiggle around the straight path. The result is a very high flux of X-rays along the wiggler beamline. An undulator is similar to a wiggler except for one point: it forces the electrons into a much weaker zigzag, so that during the entire zigzag motion synchrotron light continues to illuminate the undulator beamline. The result is a longer pulse of light rather than a series of short bursts. Without short pulses, there is no wide band of wavelengths, thus the undulator emission is not spread in a wide band but concentrated, producing high levels of flux and brightness. The picture is taken from the Elettra web site pages (<http://www.elettra.trieste.it/>).

Summarizing, some advantages of synchrotron radiation are: a wide spectra range, high photon flux, high collimation of the synchrotron light beam, spatial coherence and a possibility to choose the degree of polarization of the light.

### 2.1.3. The Elettra Synchrotron Light Source

ELETTRA is a national laboratory located in Basovizza in the outskirts of Trieste. An aerial view of the site is visible in Fig. 2.4. Its mandate is a scientific service to the Italian and international research communities, based on the development and open use of light produced by synchrotron and Free Electron Laser (FEL) sources. The light is now mainly provided by a third generation electron storage ring, optimized in the VUV and soft-X-ray range, operating with an electron energy between 2.0 and 2.4 GeV, and feeding over 25 light sources in the range from a few eV to tens of keV (wavelengths from infrared to X-rays). A fourth-generation light source based on a free-electron laser, [FERMI@Elettra](#), is currently under construction.



*Figure 2.4: Aerial view of the Elettra site (Courtesy from Aeronautica Militare Italiana, authorization RGS n.12-466 15/11/2000).*

The light is made available through a growing number of beamlines, which feed measuring stations using many different and complementary measuring techniques ranging from analytical microscopy and microradiography to photolithography. The spectral brightness available on most beamlines is up to  $10^{19}$  photons/s/mm<sup>2</sup>/mrad<sup>2</sup>/0.1%bw and the peak brightness of the FEL sources is expected to go up to  $10^{30}$  photons/s/mm/mrad<sup>2</sup>/0.1%bw. A number of support laboratories help users to prepare the set-up of their equipment and materials for best results.

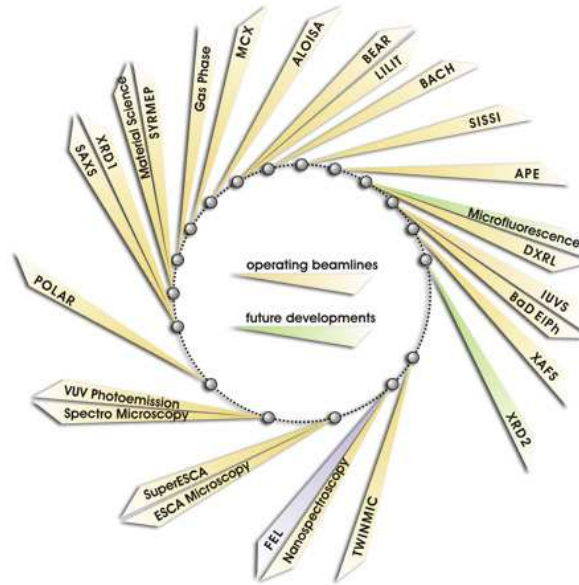


*Figure 2.5: Displacement of the beamlines at Elettra. The picture is taken from the Elettra web site pages (<http://www.elettra.trieste.it/>).*

As we can see from Fig. 2.5 the ESCAmicroscopy beamline, as many others, shares an insertion device, reducing the time available for measurement on each experimental station, but on the other hand it increases the possibility to connect more beamlines to the ring.

## 2.2. The Scanning PhotoElectron Microscope (SPEM)

In this part, the main features of the SPEM on the ESCAmicroscopy beamline are considered. The focused x-ray probe is formed using a Fresnel zone plate (Fig. 2.6), and it is this device that crucially influences the spatial resolution that can be achieved, so it is important to be aware of the main parameters that characterize these optical elements. The SPEM is itself just one part of the whole experimental station: the SPEM vacuum chamber is attached to additional vacuum chambers that provide facilities for in situ sample preparation, and other apparatus for surface characterization, such as LEED (*Low Energy Electron Diffraction*) and AES (*Auger Electron Spectroscopy*) detectors (see after for a detailed description of this techniques).

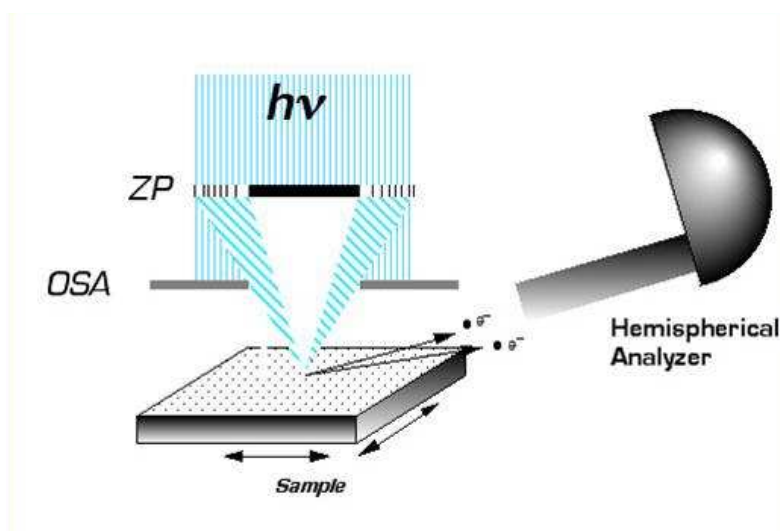


*Figure 2.6: focusing system made by a ZP and an OSA*

### 2.2.1. The SPEM Microscope at the ESCA microscopy Beamline at Elettra

The ESCA microscopy beamline was designed to implement a SPEM, to allow the investigation of laterally heterogeneous materials. The light is provided by an undulator with 81 periods (5.6 cm period) and divided in three sections.

The X-ray source covers an energy range of 200 - 1400 eV using 1<sup>st</sup>, 3<sup>rd</sup> and 5<sup>th</sup> harmonics and is optimized for the range 400 - 700 eV. The illumination is tailored to fulfill the requirements of the zone plate focusing optics using a toroidal, pre-focusing mirror and a spherical grating monochromator. The monochromator is a variable angle spherical grating monochromator with fixed entrance and exit slits. It operates in the photon energy range from 350 to 650 eV using one grating with 600 grooves/mm. The transmission is 1.1% at 400 eV. A schematic layout of the beamline is drawn in Fig. 2.7. The experimental station consists of three UHV vessels hosting the SPEM, used exclusively as a photoelectron microscope, and facilities for in-situ specimen preparation and characterization.

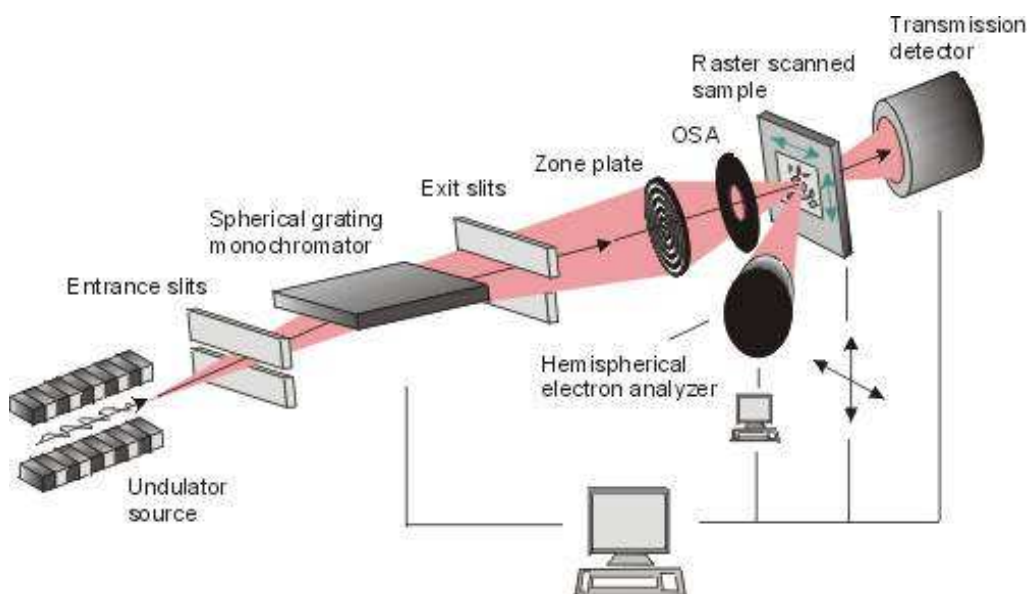


**Figure 2.7:** Scheme of the ESCA microscopy beamline. The picture is taken from the ESCAmicroscopy web pages inside the Elettra web site (<http://www.elettra.trieste.it/escamicroscopy>).

The experimental apparatus allows the user to carry out many different experiments, aiming at quantitative and qualitative chemical characterization of the surface of morphologically complex natural and fabricated materials (electronic devices, superconductors, catalysts, thin films, materials with corrosion damage, etc.), including chemical reactions and mass transport processes leading to lateral changes in the composition, morphology and electronic properties of materials.

The specimen is introduced through a fast entry air-lock and transported using magnetic arms and wobble sticks. The preparation chamber includes detectors for Low Energy Electron Diffraction (LEED), Auger Electron Spectroscopy (AES), a sputter gun, a gas inlet system, evaporation sources and facilities for sample heating.

The SPEM microscope at Elettra allows the scanning of the sample using either stepper or piezoelectric motors. The smallest step achievable with the stepper motors is 1 micron. The images acquired with these motors cover typically large areas ( $2 \times 10^4$ - $1 \times 10^5 \mu\text{m}^2$ ) and are used for the identification of the best regions that have to be measured. The time needed to complete one movement of one stepper motor (dead time) is at least 150 ms, much higher than that of the piezoelectric motor which is limited to few ms. This is the reason why most of the images during a typical spectromicroscopy experiment at the SPEM at Elettra are acquired using the

piezoelectric motors. The maximum range covered by the piezoelectric motors is  $64 \times 64 \mu\text{m}^2$ .

The smallest step that these motor can make is 5 nm, much smaller than the photon beam size. A typical image has  $100 \times 100$  or  $200 \times 200$  pixels with counting times ranging from 20 to 200 ms per pixel. It implies that the time spent for the acquisition of one image ranges from a few minutes up to one hour. The piezo motors do not suffer of the problem of backlash and then the positioning of the beam over small areas can be made easily and precisely using them.

The SPEM has two operation modes, microspot XPS spectroscopy and spectro-imaging, executed by monitoring the photoelectrons emitted within a selected energy window while rastering the sample. The spectro-imaging mode allows the reconstruction of the spectrum contained in the energy window, from micro-areas selected from the two-dimensional maps.

The core of the detection system of any SPEM is the electron analyzer. For the acquisition of the data presented in this thesis, the experimental station was equipped with an Hemispherical Electron Analyzer (HEA) from SPECS (model PHOIBOS 100) equipped with a wide angle set of electrostatic lenses and placed at  $30^\circ$  respect to the sample surface. This particular geometrical configuration enhances the characteristic surface sensitivity of the SPEM technique.

### **2.2.2. Hemispherical Electron Analyzer and Detectors**

The HEA is the type of analyzer chosen in the earliest days of XPS as most suitable for that technique, and it has remained so ever since. The basic form of a HEA is shown diagrammatically in Fig. 2.8. Two hemispheres of radii  $R_1$  (inner) and  $R_2$  (outer) are positioned concentrically. Potentials  $-V_1$  and  $-V_2$  are applied to the inner and outer hemispheres respectively, with  $V_2$  greater than  $V_1$ . The median equipotential surface between the hemispheres has radius  $R_0$  and the source S and focus F are co-linear with the centre of curvature.

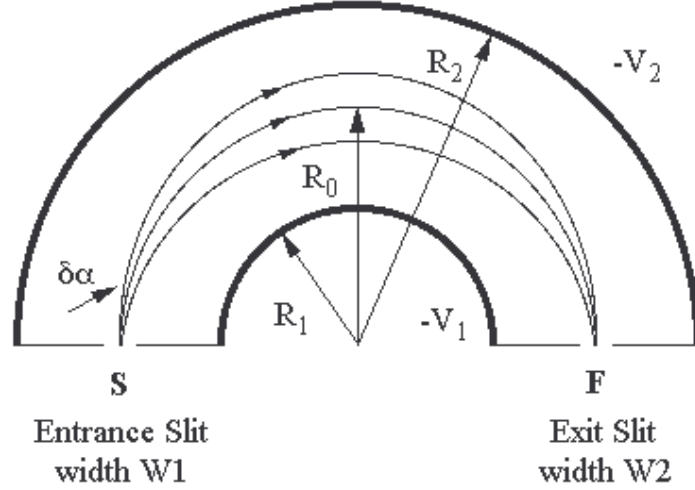


**Figure 2.8:** Schematic cross-section of a hemispherical electron analyser. Two hemispheres of radii  $R_1$  (inner) and  $R_2$  (outer) are positioned concentrically.  $R_0$  is the radius of the median equipotential surface. Potentials  $-V_1$  and  $-V_2$  are applied to the inner and outer spheres respectively, with  $V_2$  greater than  $V_1$ . The source  $S$  is located in the entrance slit of width  $W_1$  and the focus  $F$  in the exit slit of width  $W_2$ . The divergence of the electrons entering the analyser from the ideal tangential path is  $\delta\alpha$ .

The potential  $-V_0$  along the median surface is:

$$V_0 = \frac{V_1 R_1 + V_2 R_2}{2R_0} \quad (2.3)$$

If electrons of energy  $E = eV_0$  are injected tangentially to the median surface at radius  $R_0$  they will describe circular orbits of radius  $R_0$  according to the expressions:

$$V_1 = V_0 \left[ 3 - 2 \left( \frac{R_0}{R_1} \right) \right] \quad (2.4)$$

$$V_2 = V_0 \left[ 3 - 2 \left( \frac{R_0}{R_2} \right) \right] \quad (2.5)$$

from which:

$$V_2 - V_1 = V_0 \left( \frac{R_2}{R_1} - \frac{R_1}{R_2} \right) \quad (2.6)$$

$$e\Delta V = E \left( \frac{R_2}{R_1} - \frac{R_1}{R_2} \right) \quad (2.7)$$

Electrons of the correct energy  $E$ , injected tangentially at the source  $S$ , are all focused at  $F$ , for the complete hemisphere with radius  $R_0$ , i.e. for all planes through  $SF$  out of the plane of Fig. 2.8. If the electrons are injected at an angle  $\delta\alpha$  to the correct tangential direction and with an energy  $\Delta E$  different from the correct energy  $E$  than the shift  $\Delta R$  along the radius  $R_0$  from the correct focal position is then given by:

$$\Delta R = 2 R_0 \left[ \frac{\Delta E}{E} - (\delta\alpha)^2 \right] \quad (2.8)$$

I limit this presentation to the general principles without going inside the complex theory of the HEAs. A complete treatment of this matter together with the derivation of the formulas cited above can be found in Ref. [7].

Electrons at the exit slit of an HEA are counted by an electron detector. The HEA of the ESCA microscopy beamline was equipped with a multichannel electron detector (48-channels) based on channel plates as the multiplier elements and developed by the ‘Unità operativa servizio rilevatori e strumentazione’ group of Elettra.

### 2.2.3. Multichannel Detection: Spectra and Detectors

Using a 48-channel electron detector in SPEM has reduced substantially the measurement time necessary for the acquisition and the analysis of the images and has provided high efficiency, allowing with a single scan the possibility to map different chemical states and/or different elements, including the background signal as well. Fig. 2.9 shows schematically the operation of the multichannel detector. The counts collected by each channel correspond to a specific kinetic energy defined by the kinetic and pass energies at which the analyzer is set; the energy range covered by all the channels is the so-called “energy window”. Thus the 48-channel image contains 48 energy-separated images. In this way problems of misalignment, drifts of the samples or optics, short lifetime of the probed sample, etc., can be avoided.

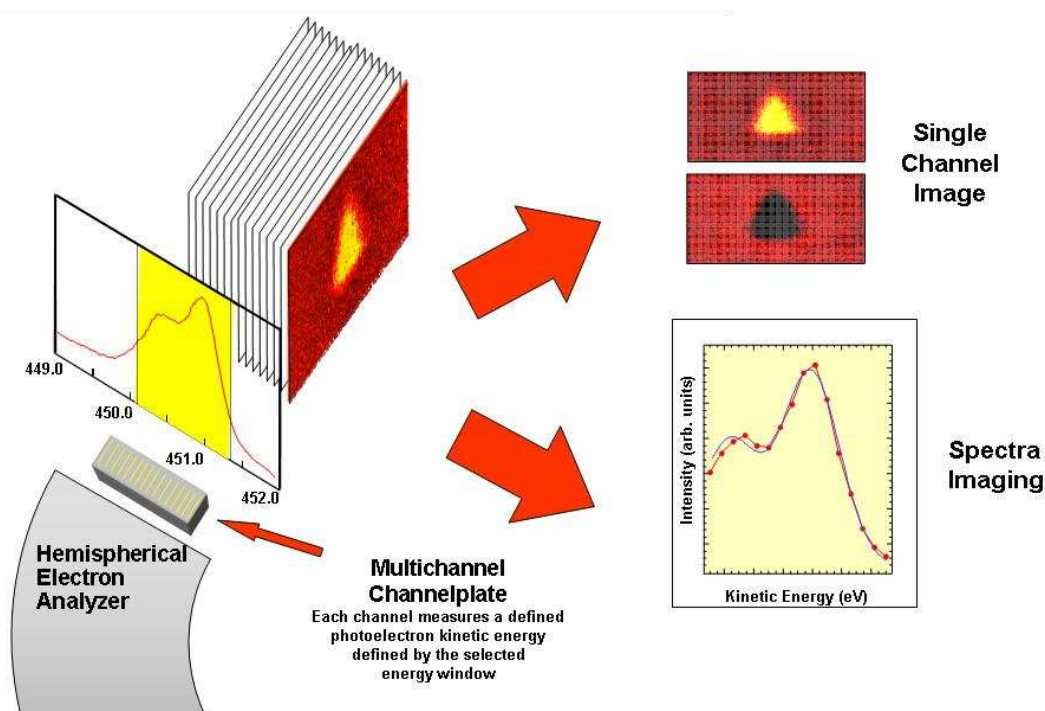


*Figure 2.9: Schematic view of the multichannel data acquisition; the 48-channel images can provide both selected energy maps and 48-points spectra from selected areas.*

The 48 signal values saved for each pixel of an image can also be used to plot a photoemission spectrum of 48 points, as illustrated in Fig. 2.9; each point corresponds to a specific kinetic energy determined by the selected energy window. These types of spectra are limited by the low number of points, but in special cases when the expected energy shifts or shape of the spectra differ substantially across the surface they can be used to extract important spectral information directly from the images.

The acquisition of the photoemission spectra with the multichannel electron detector was performed using a scanning mode; in this mode each point of the spectrum, which corresponds to a specific kinetic energy, is counted by each of the 48 anodes, thereby averaging the different sensitivity of the channels. The so-called “snapshot” acquisition mode, where each point of the spectrum is counted by only one channel and calibrated with respect to its sensitivity, was not used due to the low number of channels available. The gain in the acquisition time using a 48-channels detector with “snapshots” is in fact small with respect to the normal scanning mode.

### 2.3. Low Energy Electron Diffraction (LEED)

Low-energy electron diffraction (LEED) is a technique used for the determination of the surface structure of crystalline materials based on the bombardment with a collimated beam of low energy electrons (20-200eV) [10] and on the observation of diffracted electrons as spots on a fluorescent screen. The diffraction of low energy electrons from a crystal surface was first discovered in 1927 by Davisson and Germer [11,12]. A low voltage  $V$  accelerates the electrons towards the sample surface, where they are scattered. If we consider an electron with a momentum  $p$ , its wave function will have the following de Broglie wavelength [64]:

$$\lambda = \frac{h}{p} = \frac{h}{mv} = \frac{h}{\sqrt{2mE_{kin}}} = \frac{h}{\sqrt{2meV}} \quad (2.9)$$

where  $h = 6.626 \times 10^{-34}$  Js is the Planck constant,  $m = 9.11 \times 10^{-31}$  kg is the electron mass and  $e = 1.6022 \times 10^{-19}$  C is the elementary charge. According to this equation, the typical LEED voltages, in the range 20÷200 eV, correspond therefore to wave lengths lower than 0.3nm (i.e. of the order of interatomic distances in the crystalline sample lattice).

As shown in Fig. 2.10, a collimated and monoenergetic beam of electrons is accelerated towards the surface. Some of the impinging electrons are elastically scattered back towards the electron source. The spatial distribution of the intensity maxima (LEED pattern) of the backscattered electron stream at the electron source is determined by the surface structure. As it turns out, the positions of the intensity maxima correspond to the lattice structure of the surface in reciprocal space. Thus, the mere observation of a LEED pattern yields information about the surface structure and its long range order.

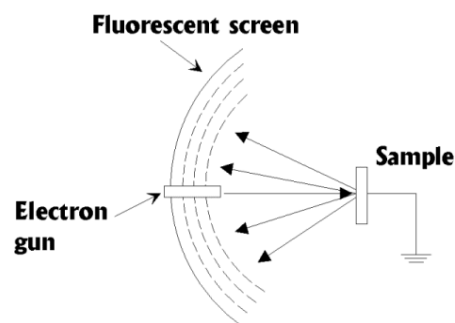


*Figure 2.10: schematic view of a LEED apparatus.*

The electron energies involved in the LEED process have a second crucial property: as shown in Fig 2.11, their inelastic mean free path is minimum: this means that low energy electrons are probing only the very topmost layers of the sample surface.

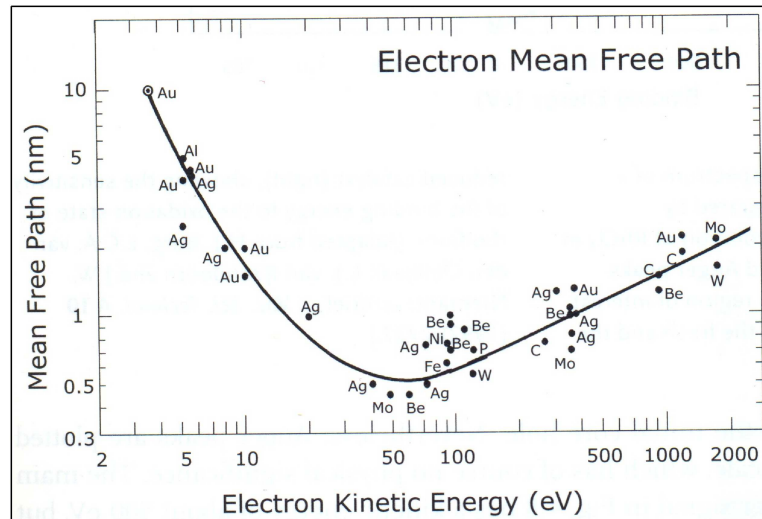


*Figure 2.11: Inelastic mean free path of electrons in solids, i.e. the mean distance that the particle can travel before being inelastically scattered in a host material and thus before losing energy.*

LEED may be used in one of two ways in routine sample cleaning and preparation procedures:

- qualitatively, where the diffraction pattern is recorded and the analysis of the spot positions gives information on the symmetry of the surface structure. In the presence of an adsorbate the qualitative analysis may reveal information about the size and rotational alignment of the adsorbate unit cell with respect to the substrate unit cell;
- quantitatively, where the intensities of diffracted beams are recorded as a function of incident electron beam energy to generate the so-called I-V curves. By comparison with theoretical curves, these may provide accurate information on atomic positions on the surface at hand.

Fig. 2.12 shows a typical LEED pattern with the reciprocal space unit cell of the surface indicated by the white rectangle.

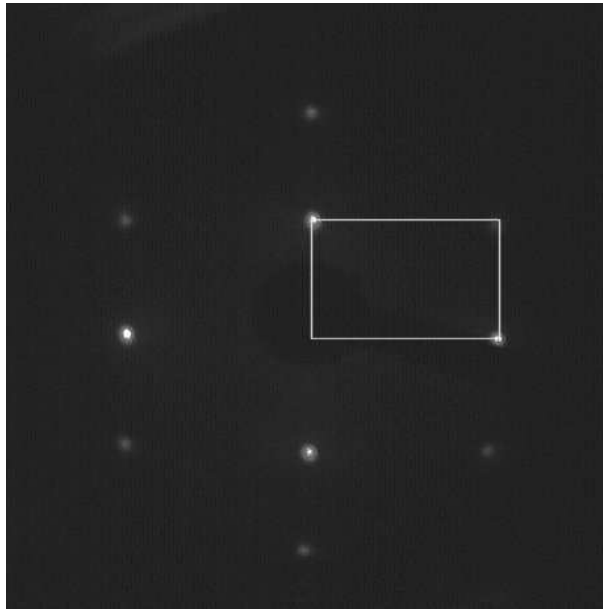


*Figure 2.12: LEED pattern of a clean Pd{110} surface at 120 K measured using electrons with kinetic energy of 140 eV.*

## 2.4. Low Energy Electron Microscope (LEEM)

LEEM is an analytical surface science technique that enables real-time observations of dynamic processes at surfaces. Such phenomena include: phase transitions, adsorption, reactions, segregation, thin film growth, strain relief, sublimation [67].

It was invented by E.Bauer in 1962, but the first working instrument was developed in 1985 by Bauer and Teliëps. As described in [13,14], low energy electron microscopy uses diffracted electron beams to get a real-space image of the surface. The microscope is capable to monitor surface structure at nanometer scale in real time. The imaging is done with a series of electromagnetic lenses and properly chosen apertures.

### 2.4.1. LEEM setup

In Fig. 2.13 the basic setup of the LEEM instrument is shown. Electrons leaving the electron gun are accelerated to an energy of several keV. These high energy electrons fly upwards, and pass a set of lenses that keep the beam position and focus them onto the sample. After passing through the beam splitter, the electrons enter the sample

chamber passing through the objective lens, being decelerated to low energy (by holding the sample at a potential close to the accelerating one). The low energy electrons are elastically backscattered at the sample surface, in the same way as in a LEED experiment. Due to the potential difference between sample surface and the objective, they are again accelerated on this path. The separator deflects the electrons back into the imaging column, where the projector lenses and the detector are located.

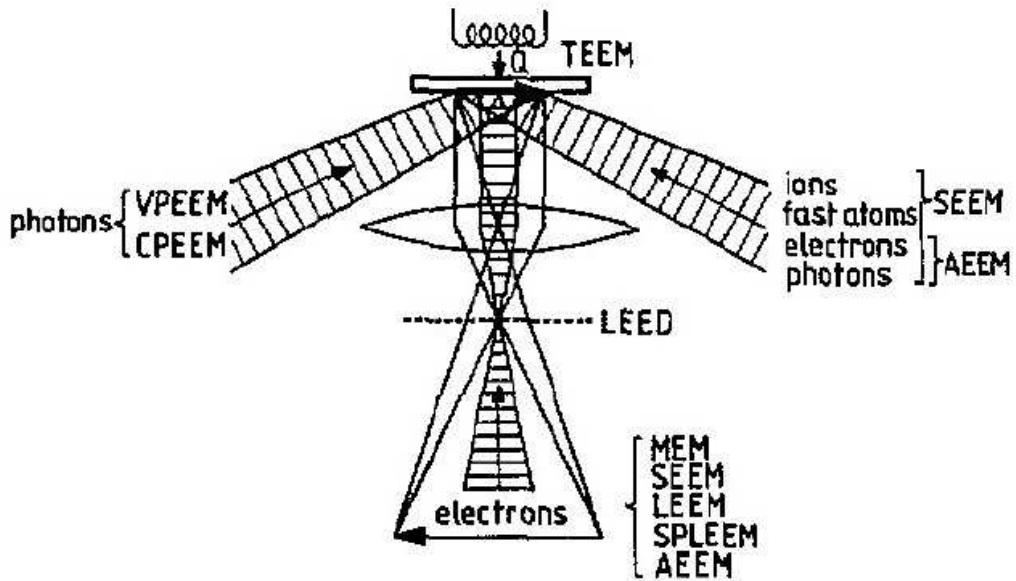


Figure 2.13: schematic representation of a Low Energy Electron Microscope [15].

### 2.4.2. LEEM methods

When the low energy electrons are scattered from the sample surface, they produce a diffraction pattern; depending on the beam that is selected, the diffraction contrast method can be used on two different ways [16]:

**Bright-field imaging:** if the specular (0,0) beam is used, “bright field” imaging is performed. In this case, the contrast is purely structural (*diffraction contrast*) and depends on the local differences in diffraction for the different surface phases present on the sample.

**Dark-field imaging:** by selecting a secondary diffracted beam, a “dark field” image of the surface is produced. Here all areas that contribute to the formation of the selected beam appear bright.

In Fig. 2.14 we report a LEED image of the W(110) surface after the adsorption of 0.5ML of oxygen: two rotational domains are formed ((1 × 2) and (2 × 1)), and choosing the red and the green spot we obtain the two darkfield imaging showing opposite contrast.

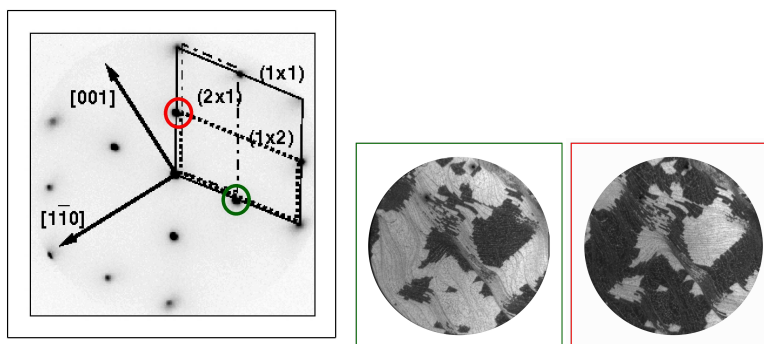


**Figure 2.14:** LEED (28 eV) and LEEM darkfield images ( $E = 9\text{eV}$ , field of view (fov) =  $10\mu\text{m}$ ) of the W(100) surface; the central and right images are acquired using the diffraction spot in green and red, respectively [17].

A LEEM instrument can be also used to image non-crystalline samples or to acquire LEED data from microscopic areas: these two methods are MEM and  $\mu$ -LEED.

If the  $\mu$ -LEED method is used, the microscope is operated as a LEED, but the probe area can be restricted to  $2\mu\text{m}$  either by inserting an aperture in the image plane in the input or exit side of the beam separator, respectively.

Our measurements have been performed with the SPELEEM microscope (Spectroscopic PhotoEmission and Low Energy Electron Microscope) at the Nanospectroscopy [16] beamline at the Elettra Synchrotron in Trieste [18, 19]. The SPELEEM combines into one single instrument a LEEM and an energy filtered X-ray photoemission electron microscope (XPEEM), therefore offering a unique combination of complementary imaging and diffraction methods. The high temporal and structural sensitivity of LEEM make it a useful complementary technique [20, 21], which helped us in understanding the morphology and the reactivity of the PtRh clusters. The best lateral resolution we could achieve in LEEM mode was  $\sim 20\text{nm}$  at 30 eV.

## 2.5. Pulsed Laser Deposition (PLD) technique

Pulsed laser deposition (PLD) is a thin film deposition technique (specifically a physical vapour deposition, PVD) where a high power pulsed laser beam is focused inside a vacuum chamber to strike a target of the material that is to be deposited. This material is vaporized from the target (in a plasma plume) which deposits it on a substrate (in our case the W(110) surface covered by an MgO thin film). This process can occur in ultra high vacuum or in the presence of a background gas, such as oxygen which is commonly used when depositing oxides to fully oxygenate the deposited films (see Fig 2.15).

While the basic-setup is simple relative to many other deposition techniques, the physical phenomena of laser-target interaction and film growth are quite complex (see the process description below).

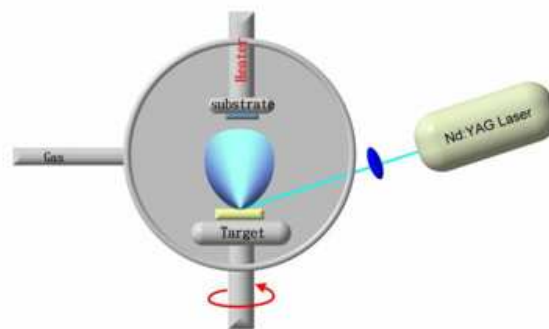


*Figure 2.15: schematic view of one possible configuration of a PLD deposition chamber.*

When the laser pulse is absorbed by the target, energy is first converted to electronic excitation and then into thermal, chemical and mechanical energy resulting in evaporation, ablation, plasma formation and even exfoliation [22]. The ejected species expand into the surrounding vacuum in the form of a plume containing many energetic species including atoms, molecules, electrons, ions, clusters, particulates and molten globules, before depositing on the typically hot substrate.

One of the fundamental premises used to justify the use of PLD, is that material transferred from an ablation target to the film is without stoichiometry deviations, but some recent studies revealed that it is incorrect even when no volatile elements are

involved [23]. The detailed mechanisms of PLD are very complex including the ablation process of the target material by the laser irradiation, the development of a plasma plume with high energetic ions, electrons as well as neutrals and the crystalline growth of the film itself on the heated substrate. The process of PLD can generally be divided into four stages:

- Laser ablation of the target material and creation of a plasma
- Dynamic of the plasma
- Deposition of the ablation material on the substrate
- Nucleation and growth of the film on the substrate surface

Each of these steps is crucial for the degree of crystallinity, uniformity and stoichiometry of the resulting film.

### **Laser ablation of the target material and creation of a plasma**

The ablation of the target material upon laser irradiation and the creation of plasma are very complex processes. The removal of atoms from the bulk material is done by vaporization of the bulk at the surface region in a state of non-equilibrium and is caused by a Coulomb explosion. In this the incident laser pulse penetrates into the surface of the material within the penetration depth. This dimension is dependent on the laser wavelength and the index of refraction of the target material at the applied laser wavelength and is typically in the region of 10 nm for most materials. The strong electrical field generated by the laser light is sufficiently strong to remove the electrons from the bulk material of the penetrated volume. This process occurs within 10 ps of a ns laser pulse and is caused by non-linear processes such as multiphoton ionization which are enhanced by microscopic cracks at the surface, voids, and nodules, which increase the electric field. The free electrons oscillate within the electromagnetic field of the laser light and can collide with the atoms of the bulk material thus transferring some of their energy to the lattice of the target material with in the surface region. The surface of the target is then heated up and the material is vaporized.

### **Dynamic of the plasma**

In the second stage, the material expands in a plasma parallel to the normal vector of the target surface towards the substrate due to Coulomb repulsion and recoils from the target surface. The spatial distribution of the plume is dependent on the background

pressure inside the PLD chamber. The density of the plume can be described by a law with a shape similar to a Gaussian curve. The dependency of the plume shape on the pressure can be described in three stages: (i) the vacuum stage, where the plume is very narrow and forward directed; almost no scattering occurs with the background gases. (ii) The intermediate region, where a splitting of the high energetic ions from the less energetic species can be observed. (iii) High pressure region where we find a more diffusion-like expansion of the ablated material. Naturally this scattering is also dependent on the mass of the background gas and can influence the stoichiometry of the deposited film.

The most important consequence of increasing the background pressure is the slowing down of the high energetic species in the expanding plasma plume. It has been shown that particles with kinetic energies around 50 eV can resputter the film already deposited on the substrate. This results in a lower deposition rate and can furthermore result in a change in the stoichiometry of the film.

### **Deposition of the ablation material on the substrate**

The third stage is important to determine the quality of the deposited films. The high energetic species ablated from the target are bombarding the substrate surface and may cause damage to the surface by sputtering off atoms from the surface but also by causing defect formation in the deposited film. The sputtered species from the substrate and the particles emitted from the target form a collision region, which serves as a source for condensation of particles. When the condensation rate is high enough, a thermal equilibrium can be reached and the film grows on the substrate surface at the expense of the direct flow of ablation particles and the thermal equilibrium obtained.

### **Nucleation and growth of the film on the substrate surface**

The nucleation process and growth kinetics of the film depend on several growth parameters including the laser parameters, like the laser fluence [ $\text{Joule}/\text{cm}^2$ ] that can affect the stoichiometry of the film [23], the surface temperature [24], the condition of the substrate surface [25] and the background pressure [26]

## 2.6. Other Techniques of Surface Science used: AES , SEM and EDX

The aim of this section is to give a brief overview of the other techniques of investigation used mainly in the preparation of the W(110) surface.

### Auger Electron Spectroscopy (AES)

AES is widely used in surface science. When an atom is ionized, following the production of a core hole by an incident electron of sufficient energy, the ion eventually loses some of its potential energy by filling this core hole with an electron from a shallower level together with the emission of energy.

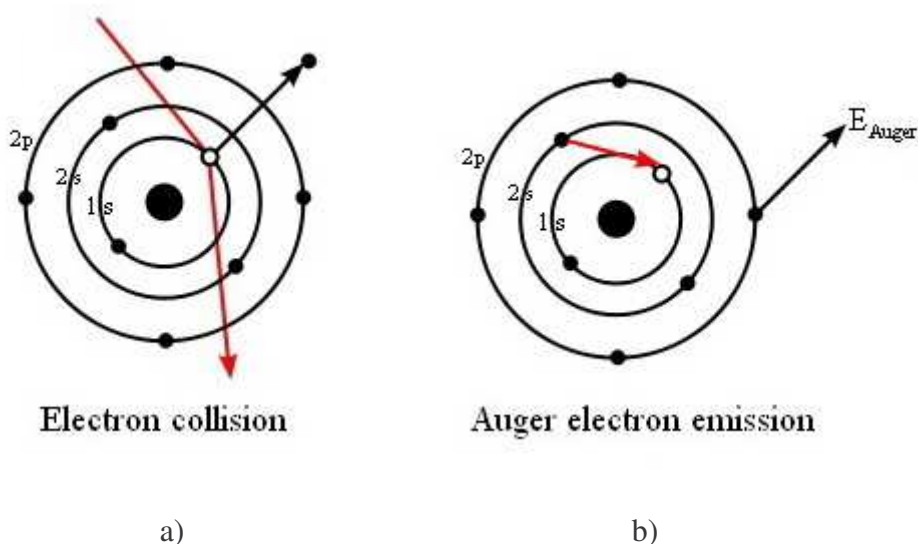


**Figure 2. 16:** an incident electron creates a core hole in the 1s level (a). An electron from the 2s level fills in the 1s hole and the transition energy is transferred to a 2p electron which is emitted (b). The final atomic state thus has two holes, one in the 2s orbital and the other in the 2p orbital.

This energy, in the case of Auger emission, appears as kinetic energy given to another shallowly bound electron. Auger electron emission is an efficient mean of filling core holes of low binding energy, thus giving rise to relatively low kinetic energy Auger electrons of short mean-free-path. Their detection outside the solid therefore provides a surface-sensitive probe of chemical composition. Although Auger electron emission,

being a three-level process, is intrinsically more complex than photoemission, its usefulness lies in the fact that it can be generated by incident electron beams and that the production, focusing and deflection or scanning of electron beams is a well-developed technology [27]. For the present case the Auger spectrum was simply used as a fingerprint of the chemical composition at the surface.

### **Scanning Electron Microscopy (SEM)**

SEM uses a focused electron beam to raster scan a sample; as the beam strikes each point on the specimen, various responses are produced due to electron-sample interactions. Several of these responses can be collected by suitable detectors to form the image. The most frequently used response in a conventional SEM is the detection of the secondary electrons generated by the primary electron beam. Secondary electrons are ejected from the sample as a result of ionization processes. The yield of these electrons depend on various factors such as the accelerating voltage applied to the primary beam electrons and the atomic number of the elements included in the sample. As the yield is very much dependent on the angle of incidence of the primary beam, topographical contrast is high.

SEMs can provide extremely high spatial resolution (less than 5 nm) and when the sample is sufficiently conductive it can often be imaged without special sample preparations.

During the present experiments a SEM Zeiss (SEM equipped with a Field Emission Gun) has been used to characterize the cluster's morphology and structure and to check for the presence of small clusters with dimensions smaller than the SPEM resolution.

### **Energy-dispersive X-ray spectroscopy (EDX)**

Energy dispersive X-ray spectroscopy (EDX) is an analytical technique used for the elemental analysis or chemical characterization of a sample, often used in conjunction with a SEM.

The EDX technique detects x-rays emitted from the sample during bombardment by an electron beam to characterize the elemental composition of the analyzed volume.

Its characterization capabilities are due in large part to the fundamental principle that each element has a unique atomic structure allowing X-rays that are characteristic of an element's atomic structure to be identified uniquely from each other. When the sample

is bombarded by the SEM's electron beam, electrons are ejected from the atoms forming the sample's surface.

The resulting electron vacancies are filled by electrons from a higher state, and an x-ray is emitted to balance the energy difference between the two electrons' states. The x-ray energy is characteristic of the element from which it was emitted.

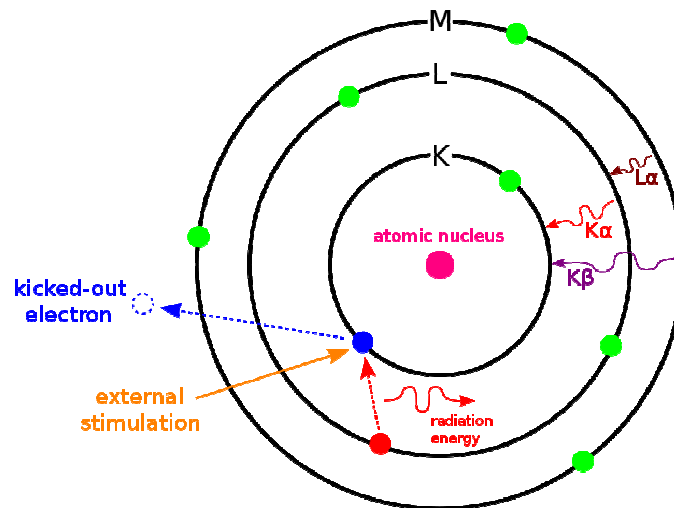


*Figure 2.17: an incident beam may excite an electron in an inner shell, ejecting it from the shell while creating an electron hole where the electron was. An electron from an outer, higher-energy shell then fills the hole, and the difference in energy between the higher-energy shell and the lower energy shell may be released in the form of an X-ray.*

Due to the multiple scattering of the electrons and x-rays inside the sample under measurement the probed depth is approximately 1-3  $\mu\text{m}$  depending from the primary electron energy. For this reason EDX analysis is considered a bulk measurement in comparison with photoemission analysis, and usually provides complementary information. Despite the electron beam is typically extremely confined ( $<10\text{ nm}$ ) the EDX signal, for the reason above mentioned, is always generated from a larger volume worsening the lateral resolution achievable.

With this technique it is possible to perform different analysis: a qualitative analysis to identify the presence of an element in the sample, quantitative analysis to quantify how much of an element we have, and it is possible to create an elemental mapping or a line profile analysis to determine the relative elemental concentration for each element versus position.

In Fig. 2.18 an EDX spectrum taken on a PtRh micro-sized particle is reported: the peaks correspond to the energetic positions of the Pt and Rh emission lines.

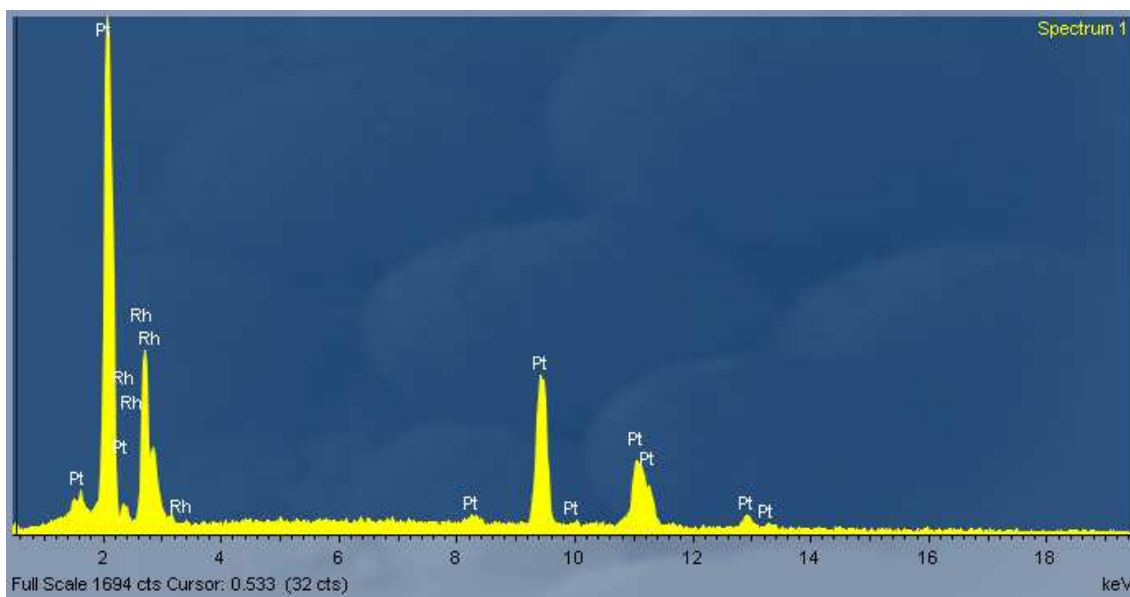


*Figure 2.18: EDX spectrum taken on a micro-size PtRh cluster.*

## 2.7. Micro Wave Plasma source

Microwave energy is used to create a gas plasma from which ions are extracted. In the setup used for the experiments reported in this work microwaves with a frequency of 2.45 GHz are generated by a microwave magnetron and coupled through a resonant coupler into a coaxial feedthrough structure which guides the microwaves into the vacuum and up to the Boron Nitride (BN) or Alumina plasma chamber. A plasma is excited in the chamber and the microwaves absorbed. The plasma is physically confined by the chamber and occurs there preferentially due to the higher local gas pressure.

Further enhancement of the plasma density is provided by a magnetic quadrupole arranged around the discharge chamber. This generates an 87 mT field inside the plasma at which strength, electrons in a 2.45 GHz microwave field will undergo electron cyclotron resonance motion. This spiralling motion greatly enhances the electron path length and therefore the probability of collision with other molecules and subsequent ionisation.



*Figure 2.18: the Tectra Gen2 Plasma Source mounted at the ESCA microscopy beamline.*

The open end of the plasma chamber is closed with a grid of holes. When operated as an ion source, the grid is made from molybdenum or other materials. Positive voltage applied to this grid accelerates ions from the plasma out into the chamber. An additional grid is provided to assist with ion extraction and beam current control. It also helps preventing electron back-streaming where an ion beam neutraliser is employed.

When the instrument is operated as an atom source or plasma source, the metal grids are replaced by aperture plates (BN or Alumina) with a number of small holes.

The specially designed aperture plate inhibits ions from escaping from the plasma, yet allows reactive neutrals to escape and form the dominant beam fraction. The emitted particles are largely thermalised through multiple collisions on passing through the aperture. These neutrals have proven to be very effective in low damage surface treatments such as nitridation and oxidation. [28, 29]

The further addition of an ion-trap option can completely remove the residual ion content from the beam where this may be of concern.

A hybrid mode is also available in which metal and dielectric grids are combined to produce a source which functions principally as an atom source but where a small ion current can also be added to the beam.

## References

---

1. Robinson, H. and Rawlinson, W. J. *Philosophical Magazine* **1914**, 28, 277.
- 2 Robinson, H. *Philosophical Magazine* **1925**, 50, 241.
- 3 Siegbahn, K. et al. "ESCA: atomic, molecular and solid state structure studied by means of electron spectroscopy,, **1967**, Almquist and Wilsells, Uppsala.
- 4 Himpsel, F. J. *Surf. Sci.* **1994**, 299, 525.
5. Pehlke, E.; Scheffler, M. *Phys. Rev. Lett.* **1993**, 71, 2338.
- 6 Osten, H. J.; Methfessel, M.; Lippert, G.; Rucker, H. *Phys. Rev. B* **1995**, 52, 12179.
- 7 Briggs, J.; Seah, M.P. "Practical Surface Analysis" Wiley, **1990**.
- 8 "Handbook on Synchrotron Radiation" edited by Ernst-Ekhard Kock – North Holland (**1983**).
- 9 "Synchrotron Radiation Research" edited by H. Winick – S. Doniach – Plenum Press (**1980**).
10. Oura, K.; Lifshits, V.G.; Saranin, A.A.; Zotov, A.V.; Katayama, M. *Surface Science* **2003** Springer-Verlag, Berlin Heidelberg New York. pp.1–45.
- 11 Christmann, K. Introduction to Surfaces Physical Chemistry, **1991**.
- 12 Ertl, G.; Kupperts, J. Low Energy Electrons and Surface Chemistry, Verlag Chemie, **1985**.
- 13 Bauer, E. Ultramicroscopy **1985**, 17, 51.
- 14 Bauer, E. *Surface Review and Letters* **1998**, 5, 1275.
- 15 Bauer, E. *Rep. Prog. Phys.* **1994**, 54, 895-938.
- 16 URL <http://www.elettra.trieste.it/nanospectroscopy>.
- 17 Mentès, T. O.; Stojic, N.; Binggeli, N.; Locatelli, A.; Aballe, L.; Kiskinova, M.; Bauer, E. *Phys. Rev. B* **2008**, 77, 155414.
- 18 Schmidt, T.; Heun, S.; Slezak, J.; Diaz, J.; Prince, J.C.; Lilienkamp, G.; Bauer, E. *Surface Review and Letters* **1998**, 5, 1287.
- 19 Günther, S.; Kaulich, B.; Gregoratti, L.; Kiskinova, M. *Progr. Surf. Sc.* **2002**, 70, 187.
- 20 Locatelli, A.; Sbraccia, C.; Heun, S.; Baroni, S.; Kiskinova, M. *Journal of the American Chemical Society* **2005**, 127, 2351.
- 21 Locatelli, A.; Mentès, T.O.; Aballe, L.; Mikhailov, A.; Kiskinova, M. *The Journal of Physical Chemistry B Letters* **2006**, 110, 19108.

- 22 Chrisey, D.B.; Hubler, G.K. Pulsed Laser Deposition of Thin Films, edited by, John Wiley & Sons, **1994**
- 23 Ohnishi, T. et al. *Journal of Applied Physics* **2008**, 103, 103703
- 24 Ferguson, J.D. et al. *Phys. Rev. Lett.* **2009**, 103, 256103.
- 25 Koster, G. et al. *Applied Physics Letters* **1998**, 73, 2920.
- 26 Ohtomo, A.; Hwang, H.Y. *Journal of Applied Physics* **2007**, 102.
- 27 Woodruff, D.P.; Delchar, T.A. “Modern techniques of surface science”, Cambridge, **1994**.
- 28 Schmidt, A.A.; Offermann, J.; Anton, R. *Thin Solid Films* **1996**, 281-282, 105-107.
- 29 Anton, R.; Wiegner, T.; Naumann, W.; Liebmann, M.; Klein, C.; Bradley, C. *Rev.Sci.Instr.* **2000**.

# Chapter 3

## Sample preparation and characterization

As previously stated in the introduction, one of the fastest-developing fields in surface science is research on nanoclusters of semiconducting and metallic materials. The latter have been studied in many different ways: as free clusters, as embedded in a host matrix or as deposited onto a support. The last type is certainly the most relevant for real-world heterogeneous catalysis applications.

A typical supported metal catalyst is usually deposited on a thermally stable and surface-rich oxide support material, such as alumina ( $\text{Al}_2\text{O}_3$ ), magnesium oxide ( $\text{MgO}$ ) or silica ( $\text{SiO}_2$ ). On these oxides, well-dispersed metal particles typically in the size range of a few nanometers are prepared via, for example, impregnation of a precursor followed by suitable chemical and thermal treatment (though other methods exist). The role of the support is well described in the literature [1] and is based on several effects. The first is the modification of nanoclusters' electronic properties induced by the particle-support interactions. The second is the diffusion of the reactants through the surface.

One of the best choices for modelling real oxide-supported catalysts using the surface science approach is the deposition of nanoclusters on an ultra-thin oxide film, which in turn is supported by a conductive material.

The choice of the supported thin films is a compromise between two needs. First of all, we wish to model a real catalyst composed by metal particles supported by a metal

oxide. However, performing measurements on metal nanoclusters on an oxide support is non-trivial, because almost all metal oxides are nonconductive. Most surface science experimental techniques (XPS, STM and in general all electron microscopies and spectroscopies) cannot be easily employed if the support is an electrical insulator: the sample undergoes charging, which strongly influences the measurements. Metal oxide thin films represent one solution to this problem. It has been shown that even films with a thickness of just a few angstroms can exhibit physical properties characteristic of the bulk material. [2, 3] Using an oxide layer of a thickness between 10 and 20 Å, supported by a metal substrate, we obtain two critical desirable characteristics:

- support conductivity: the metal substrate is naturally conductive, and the oxide thin film becomes practically conductive because the reduced thickness opens a significant tunneling channel.
- real oxide behaviour: the oxide layer is thick enough to isolate the surface from metallic substrate influence so the nanocluster support is an almost real oxide.

Of course the creation of this oxide/metal support depends critically on the choice of the metal substrate, which must be done in a way so as to match the two lattice constants and to create understandable interactions between the two materials.

Many investigations have been conducted on MgO supported nanoclusters, focusing on both electronic and structural properties, as well as chemical reactivity as in the case of Pd [4] and Au [5] nanoclusters.

For the reasons explained above, PtRh clusters were deposited on an ultrathin 2-3 nm MgO film grown on the (110) surface of a tungsten single crystal.

W(110) sample was cleaned in UHV by Ar ion sputtering followed by annealing at 990°C in a pressure of  $2 \times 10^{-8}$  mbar for one day, followed by a number of fast annealing, in UHV and in presence of oxygen ( $10^{-6}$  mbar), till a temperature of 1775° C for removing completely the presence of carbon and oxygen. This check was performed by means of AES measurements. A final LEED measure was made for inspecting the surface reconstruction.

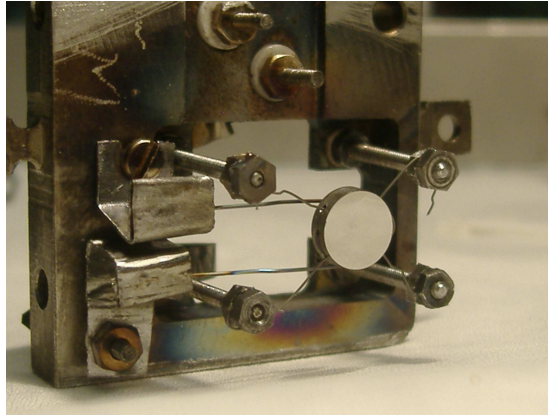


*Figure 3.1: W(110) single crystal sample mounted on the sample holder*

The MgO films were prepared by growing first a thin epitaxial Mg layer on the clean W(110) sample at RT in UHV for 5 min (the deposition rate of Mg was  $\sim 0.5$  ML/min), followed by a deposition of Mg in oxygen ambient ( $3 \times 10^{-6}$  mbar) for other 15 min.

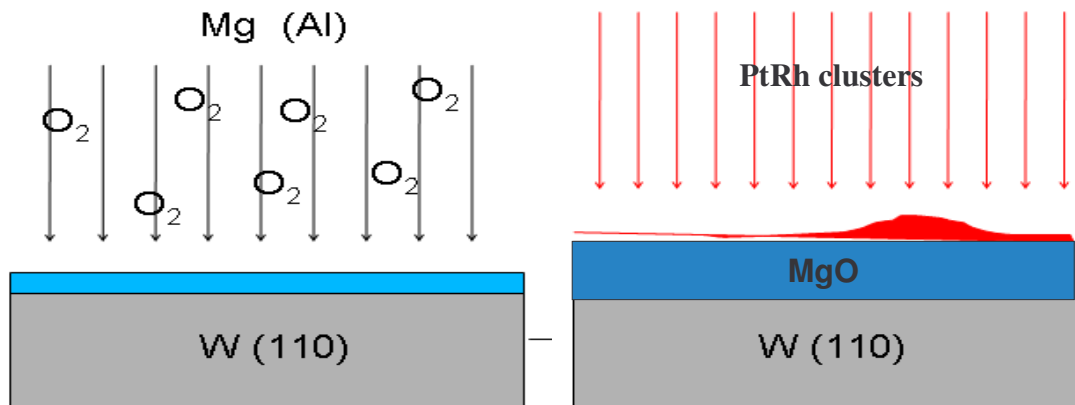


*Figure 3. 2: sketch of the MgO deposition. MgO films were prepared by growing first a thin epitaxial Mg layer on the clean W(110) sample at RT in UHV for 5 min (the deposition rate of Mg was  $\sim 0.5$  ML/min), followed by a deposition of Mg in oxygen ambient ( $3 \times 10^{-6}$  mbar) for other 15 min. After that PtRh clusters were deposited by PLD.*

The catalyst layer was prepared via Pulsed Laser Deposition by ablating a Pt<sub>50</sub>Rh<sub>50</sub> target with a Nd:YAG laser operated at 10 Hz repetition rate and 10 ns pulse width. The ablated platinum-rhodium target was placed in the focal spot of the focusing optics illuminated with both 532 and 1064 nm harmonics of the laser. The calibration

performed with 1 micron aperture and power meter has estimated the fluency at  $10 \text{ J/cm}^2$ , which is fairly above the laser ablation limit. Cluster's deposition was made at a background pressure of  $3 \times 10^{-7}$  mbar and for 10 seconds.

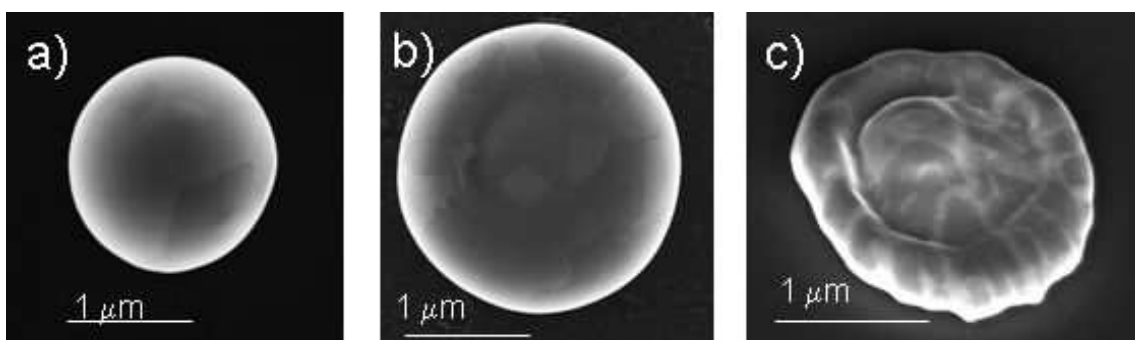


*Figure 3.3: image of the  $\text{Pt}_{50}\text{Rh}_{50}$  target. The effects of the laser ablation on the surface are clear visible.*

After the deposition, the sample with the PtRh clusters of different dimensions was annealed at 500 K in  $\text{H}_2$  environment ( $P = 1.2 \times 10^{-7}$  mbar) for 48 hours in order to ensure the complete reduction of the surface.

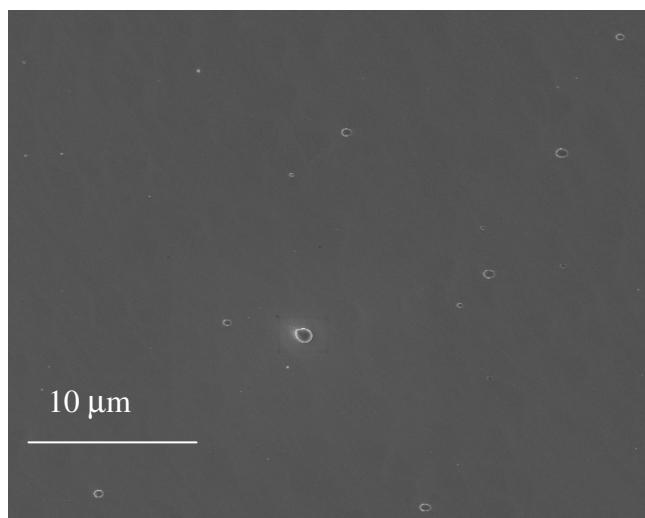
The deposition procedure for reproducible sample preparation was established by ex-situ characterization of the particle morphology and distribution by atomic force microscopy (AFM) and secondary electron microscopy comparing a large number of samples.

Fig.3.4 shows 3 SEM pictures of clusters; pictures a) and b) clearly show the surface segmentation with crystals/facets ranging from 10nm to hundreds of nm while particle c) is characterised by a different morphology.



*Figure 3.4: SEM pictures at 5 KeV of PtRh particles as deposited, a) and b) with football-like shape, c) with a different morphology*

The chosen deposition parameters resulted in a low particle density, approximately 1 particle/ $10^4 \mu\text{m}^2$  for particles of size between 50-1000 nm, while the density of the smaller ones ( $< 50$  nm) was below the critical value for producing a continuous film.



*Figure 3.5: low magnification SEM image of the surface of the sample after a PLD deposition.*

As shown in Fig.3.5, this particle distribution allowed us to investigate the behaviour of isolated single particles excluding any proximity interaction effect.

The AFM and SEM characterization of samples showed that approximately 10% of the MgO support surface is covered with nano-particles of average size around 5 nm (see Fig. 3.6), whereas the particles larger than 100 nm, which were detectable also with SPEM, are a minority.

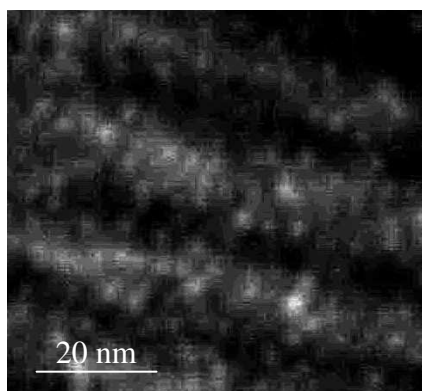


*Figure 3.6: high magnification SEM image of the surface of the sample around the big particles. Small clusters with an average size of 5 nm cover approximately 10% of the surface*

According to the statistical analysis of the shapes the football-like (Fig. 3.7a) and volcano-like (Fig. 3.7b) ‘large’ particles are almost equally distributed. The intensity variations of the high-resolution SEM images in Fig. 3.7 indicate that both types of ‘large’ particles have a similar complex morphology with well-defined uniform regions composing a puzzle on the particle surface.

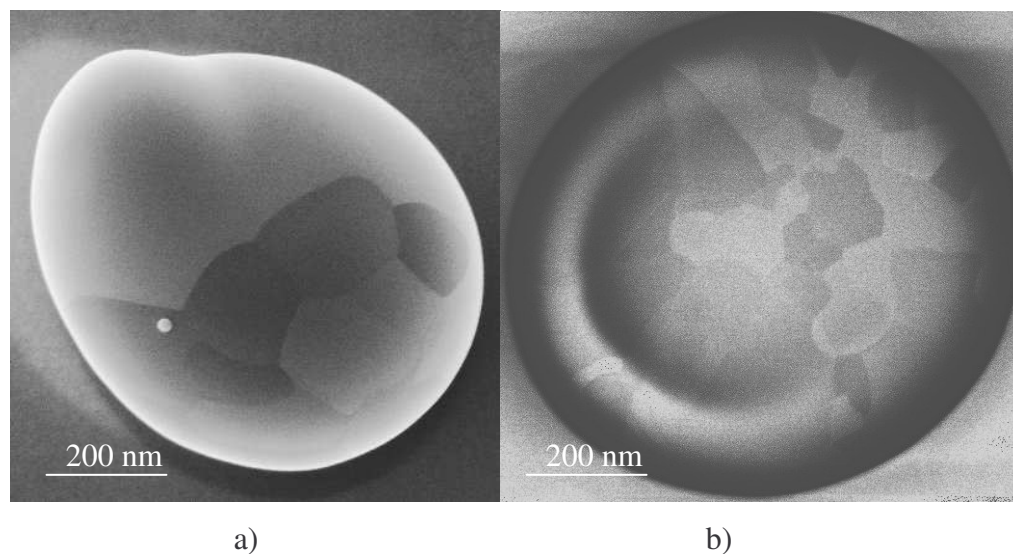


*Figure 3.7: SEM images of islands with accentuated (a) a football-like (b) donut-like shape*

Since along with topography the local surface structure can also contribute to the SEM contrast, this suggests coexistence of regions with a different plane orientation, which was confirmed by the LEEM measurements, described in the next chapter. Apparently, the surface morphology of both ‘large’ particles accounts for the very similar chemical and structural evolution we observed under oxidation conditions.

Due to the deposition process of the particles also the surface of the bigger ones is covered by the smaller clusters. We tried to find the presence of that nano-sized particles on the surface of the larger ones acquiring high resolution SEM and AFM images. In both cases it was not possible to reveal the presence of such small clusters. We are confident that the reason must be attributed to the pronounced topography which characterises the particles which artificially modify the contrast in the acquired images (SEM) or makes almost impossible to perform a continuous and linear scan (AFM); the geometry of the tip of the AFM is indeed not compatible with the spherical shape of the

clusters as we can see in Fig.3.8. In the flat region, in fact, as shown above the small clusters are well visible (see Fig. 3.6).

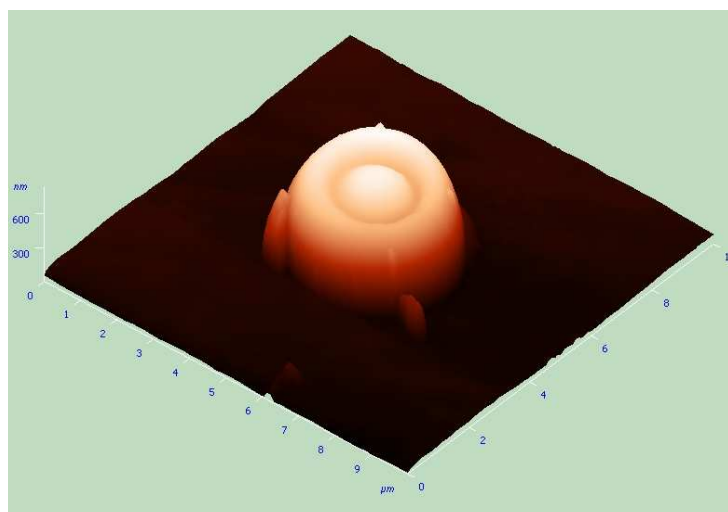


**Figure 3.8:** AFM 3D image taken on a big particle in non-contact mode.

Fig. 3.9 shows an AFM phase image taken on a big cluster. This kind of images gives information mainly on the main morphology of the particles. Even by using the non-contact image acquisition mode it was very difficult to distinguish in the images the presence of the well ordered facets as clearly viewed in the SEM pictures. In Fig. 3.9 one of these images has been shown. Despite the main borders of the particle are seen and changes in the contrast occur in the central part of the cluster it is almost impossible to relate such contrasts to the oriented facets.

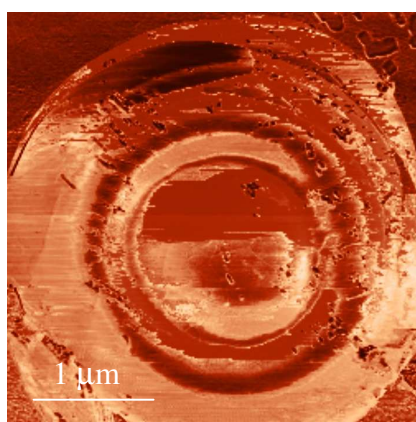


**Figure 3.9:** AFM phase image of a big cluster in non-contact mode

## References

- 1 Libuda, L.; Freund, H.-J. *Surf. Sci. Rep.* **2005**, 57, 157.
- 2 Freund, H.-J. *Phys Status Solid B* **1995**, 192, 407.
- 3 Schintke, S.; Messerli, S.; Pivetta, M.; Patthey, F.; Libioulle, L.; Stengel, M.; De Vita, A.; Schneider, W.-D. *Phys Rev Lett* **2001**, 87, 276801.
4. Nolte, P.; Stierle, A.; Balmes, O.; Srot, V.; van Aken, P.A.; Jeurgens, L.P.H.; Dosch, H *Cat. Today* **2009**, 145, 243.
5. Yulikov, M.; Sterrer, M.; Heyde, M.; Rust, H.-P.; Risse, T.; Freund, H.-J.; Pacchioni, G. ; Scagnelli, A *Phys. Rev. Lett.* **2006**, 96, 146804.

# Chapter 4

## Oxidation states of single particles monitored by SPEM

### 4.1. Working conditions

The chemical characterization of the PtRh particles deposited on the MgO film was performed with the scanning photoemission microscope (SPEM) described in chapter 2. Under the experimental conditions the lateral resolution was better than 100 nm in the imaging mode and ~160 nm in microspot spectroscopy. The measurements were carried out using 640 eV photon energy and overall spectral energy resolution of 220 meV in microspot spectroscopy and ~320 meV (Rh) and 490 meV (Pt) in spectroimaging mode. For the deconvolution of the Pt and Rh core-level spectra the well-developed procedure with Doniach-Sunjic functions convoluted with Gaussians was used, accounting for the experimental resolution and broadening due to different factors. [1]

For the oxidation of the samples we used an atomic oxygen plasma source, as the one described in chapter 2, which allowed us to reach advanced oxidation states keeping the background O<sub>2</sub> pressure below 10<sup>-5</sup> mbar. The upper limit of the atomic oxygen flux in the vicinity of the sample surface was estimated to be ~ 10<sup>13</sup> atoms/s × cm<sup>2</sup>. The overall oxygen dose was controlled by the exposure time.

### 4.2. Results

In both Rh 3d<sub>5/2</sub> and Pt 4f<sub>7/2</sub> maps, which provide identical shape-size-morphology information, the ‘large’ PtRh particles, covering a very small fraction of the support,

appear as distinct bright features. Fig. 4.1 is a large scanning SPEM map taken on the Pt energy where it is possible to identify bright islands that correspond to a big PtRh clusters. Once one of them is found it is possible to focus on it and perform more detailed image and acquire spectra.

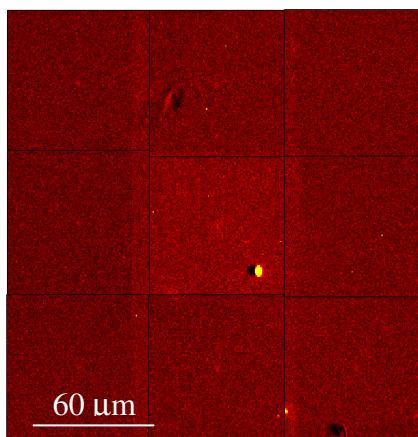


**Figure 4.1:** SPEM image taken at the Pt energy. The brighter island is a PtRh micro sized cluster.

The areas surrounding the ‘large’ particles are covered with non-resolvable by SPEM nano-particles and appear flat in the Rh and Pt maps with weak variations in the contrast level reflecting a non-uniform cluster density. According to a simple calculation the very low Rh  $3d_{5/2}$  and Pt  $4f_{7/2}$  intensity in these regions suggests that the nano-particles cover less than 10% of the MgO surface.

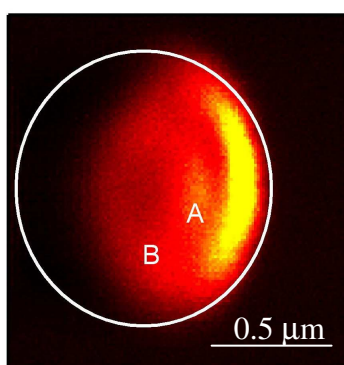


**Figure 4.2:** Pt 4f map of a single micro-particle. The white circle highlights the real size including the shadowed region at the left. Positions labeled A and B indicate the points where the spectra reported in the next figures were measured. This particle is characterized by a complex morphology, resulting in sensible contrast variations in the SPEM images.

As will be shown later there is a direct correlation of the morphology variations to the reactivity of the different particle regions. It should be noted that the brightest and darkest regions on the right and left hand side of the particle are artefacts due to height-related enhancement and shadowing of the emitted photoelectrons, respectively. [2]

The Rh $3d_{5/2}$  spectra of the particle in Fig. 4.2, taken before and after two oxidation cycles are summarised in Fig. 4.3 and compared to the spectra acquired on the surrounding “flat” regions covered with nano-particles.

The Rh  $3d_{5/2}$  spectra measured at different regions of the reduced particle have identical shapes and intensity spread corresponding to the contrast variation in the Fig. 4.2. The best deconvolution of these spectra requires two components at binding energy (BE) 307.2 eV and 306.8 eV, in fair agreement with 307.1 eV and 306.6 eV values, reported for PtRh(100), as bulk and surface components, respectively. [3] However, compared to the Rh  $3d_{5/2}$  spectra of a well-ordered PtRh(100) alloy the ones of the particles are broader, and the surface component is very weak, indicating that the coexisting differently oriented planes have a poor long range order or very small dimensions. As a reference for the energy position of metallic Rh, which remains unchanged in the PtRh alloy [3], we show in the bottom of panel (a) the Rh  $3d_{5/2}$  spectrum of a Rh(100) single crystal, measured with our experimental setup. The spectrum from the ‘flat’ region with a maximum at 307.7 eV represents the averaged spectrum of nano-particles of variable sizes. Accordingly, it is very broad and without statistical analysis of the particle size distribution any tentative deconvolution is speculative. However, the higher binding energy of the peak maximum suggests dominance of clusters smaller than 10 nm, when the size starts to exert sensible initial and final state effects on the energy of emitted core level electrons. [4]

The evolution of the Rh $3d_{5/2}$  spectra taken from different spots on the ‘large’ particles upon oxidation showed sensible site dependence. The lateral heterogeneity of the oxidation states developed within the same micro-particle is represented better by the two spectra recorded in the selected spots (A and B) indicated in Fig. 4.2. We would like to note that these spectra represent only two regions of the complex oxidation anisotropy of the particle, which is revealed by the chemical maps described below.

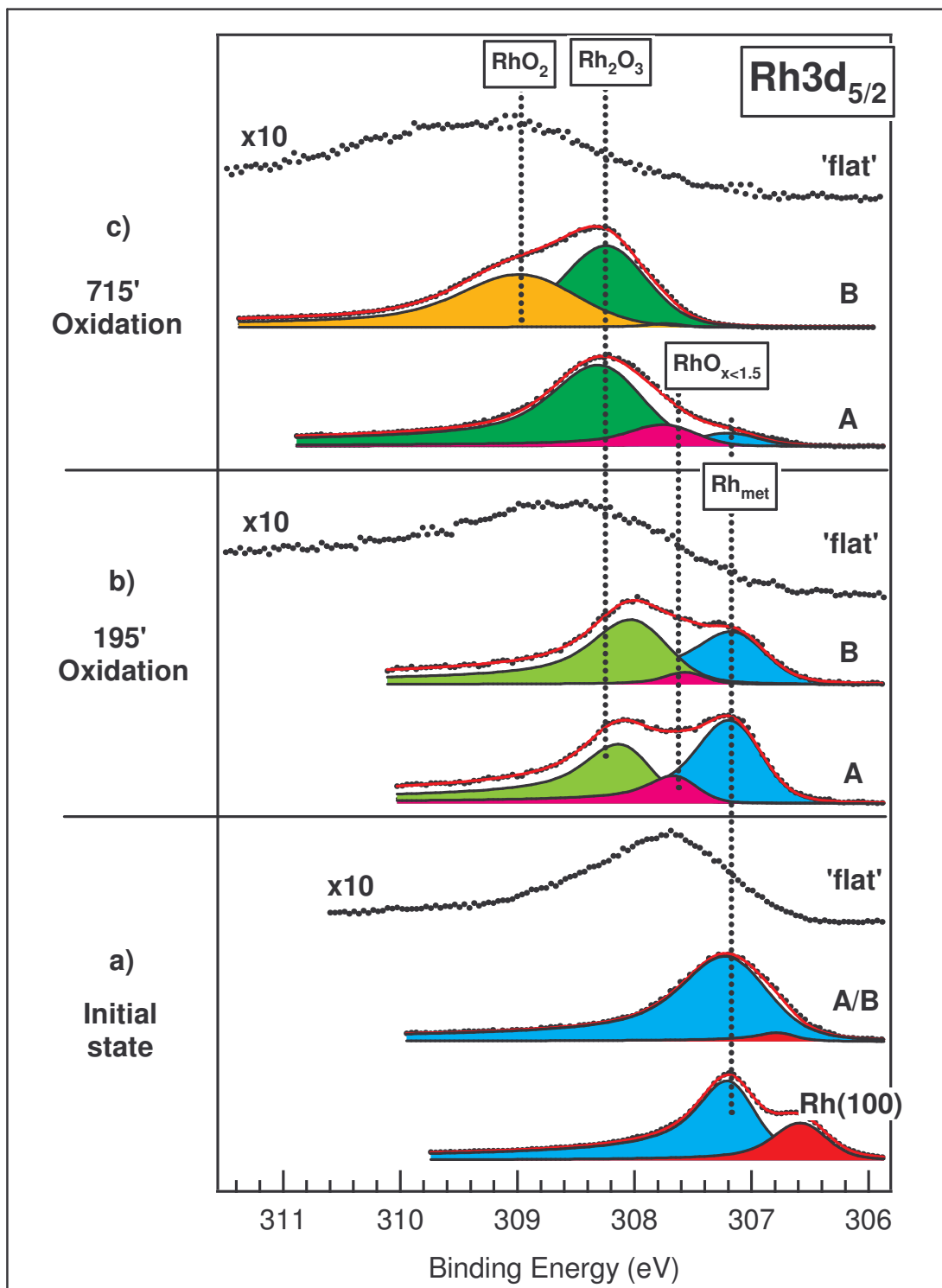


**Figure 4.3:** Rh  $3d_{5/2}$  spectra acquired in points A and B as indicated in Fig.4.2 and in a 'flat' region covered with nano-particles: (a) before exposing to atomic oxygen; (b) after 195' exposure (dose of  $\sim 10^{17}$  at.cm<sup>2</sup>); (c) after 715' exposure (dose of  $\sim 4 \cdot 10^{17}$  at.cm<sup>2</sup>). The Rh  $3d_{5/2}$  spectrum of a clean Rh(100) single crystal is shown in the bottom as an energy reference. The energy positions of the main components considered in the deconvolution of the spectra are indicated with dashed lines.

After the first oxygen dose of 195' (Fig.4.3 -panel (b)) the deconvolution of Rh3d<sub>5/2</sub> spectra requires three components: one metallic and two peaked at higher BE, 307.6-307.7 eV and 308.1-308.2 eV, respectively. In accordance with previous studies [5], the first peak can be assigned to surface oxide, RhO<sub>x</sub>, while the highest BE one indicates the growth of a Rh<sub>2</sub>O<sub>3</sub> phase, becoming more pronounced with advancement of the oxidation process. By comparing the spectra taken in points A and B, it is obvious that the region B is in a more advanced oxidation state. The different local activity of the different particle regions towards oxidation becomes more evident at higher oxygen exposure (715') when the metallic component is completely suppressed and a new component at 309.0 eV, assigned to a RhO<sub>2</sub> state, emerges in the spectrum from region B, while in region A the Rh<sub>2</sub>O<sub>3</sub> component becomes dominant.

Accordingly, the spectra from the 'flat' region become broader and shift towards higher BE. The actual oxidation state of the nano-particles cannot be well defined, since the size-induced shift is not necessarily the same for metallic and oxidized states. However, after the second dose the energy window of the spectra indicates that the nano-particles are fully oxidized and higher oxidation states dominate.

The corresponding evolution of the Pt 4f<sub>7/2</sub> spectra upon oxidation is shown in Fig. 4.4 Here, as a reference for the Pt metallic component we measured the Pt(111) single crystal surface, where the surface component is poorly resolved due to limited spectral resolution. As can be expected, the Pt 4f<sub>7/2</sub> spectrum of the particle in the initial state requires a single bulk component at 71.0 eV. Similar to the Rh 3d<sub>5/2</sub> spectra, the Pt 4f<sub>7/2</sub> spectra from the 'flat' area are also very broad and shifted to higher BE with a maximum at 71.6 eV. Compared to the Rh 3d<sub>5/2</sub> spectra the Pt 4f<sub>7/2</sub> ones undergo less dramatic changes upon oxidation, in accordance with the lower affinity of Pt to oxygen. The metallic component remains dominant even after the highest oxygen dose which indicates that only the Pt top layers are oxidised. After the first oxygen dose, the oxidation-related new components at 71.75 eV and 72.05 eV, respectively, are more pronounced in the B region spectra. They can be tentatively assigned to the PtO<sub>x<1</sub> transient surface oxide and PtO phases, in accordance with the previous reports [6, 7]. The Pt spectra undergo more dramatic changes after the second oxygen dose, when a third component at 73.0 eV grows as well.

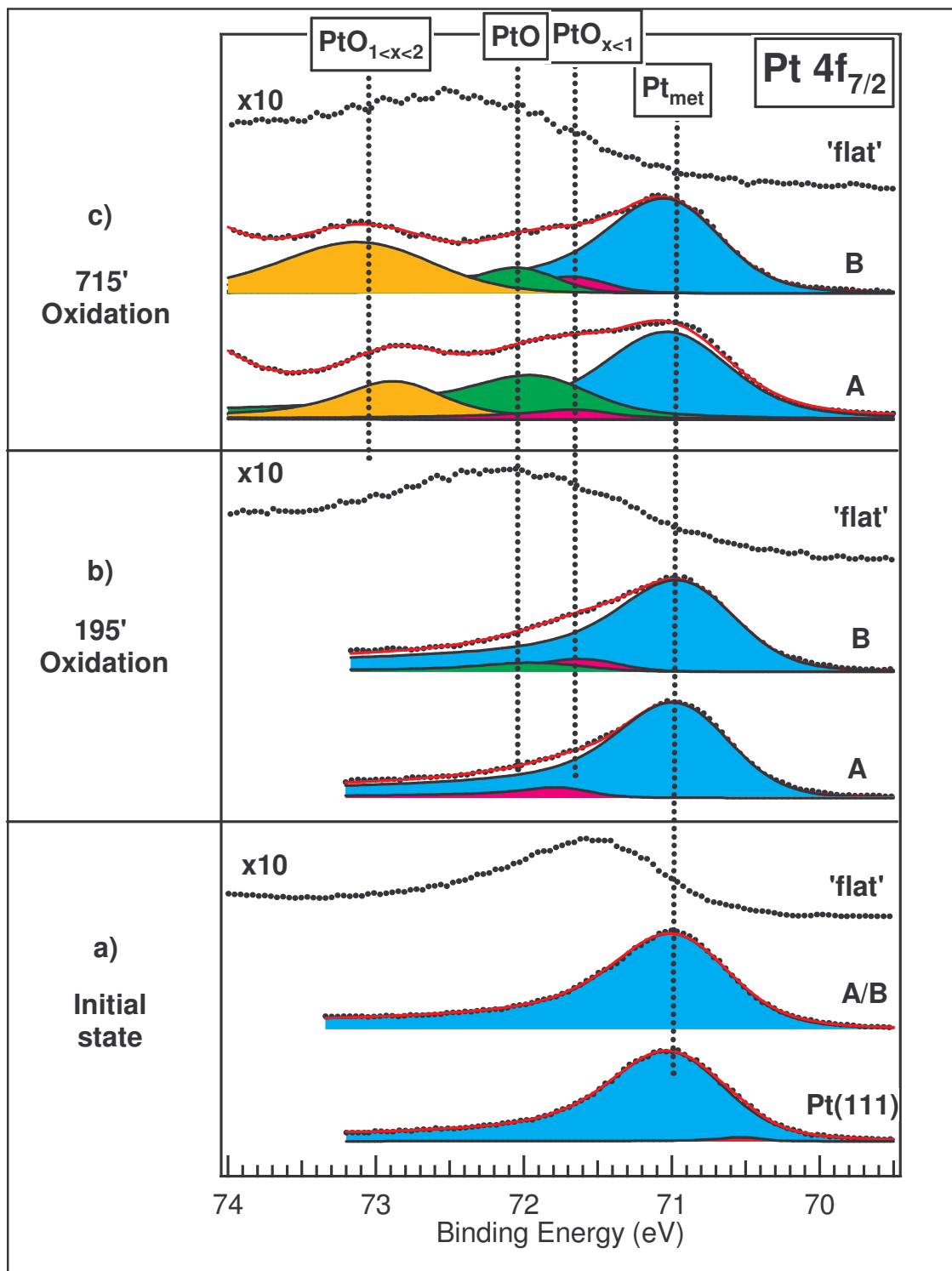


**Figure 4.4:** Pt  $4f_{7/2}$  spectra acquired in points A and B indicated in Fig. 4.1 and in a 'flat' region covered with nano-particles: (a) before exposing to atomic oxygen; (b) after 195' exposure (dose of  $\sim 10^{17}$  at.cm<sup>2</sup>); (c) after 715' exposure (dose of  $\sim 4.10^{17}$  at.cm<sup>2</sup>). The Pt  $4f_{7/2}$  spectrum of a clean Pt(111) single crystal is shown in the bottom as for energy reference. The energy positions of the main components considered in deconvolution of the spectra are indicated with dashed lines.

Since this BE is lower than the one reported for the PtO<sub>2</sub> phase  $\geq 73.5$  eV,[6, 7] we tentatively attribute this state to a transient PtO<sub>1<x<2</sub> phase. The higher weight of the 73.0 eV component in the spectrum from the B region confirms the site-dependent oxidation trend evidenced by the Rh 3d<sub>5/2</sub> spectra in Fig. 4.3. The evolution of the Pt 4f<sub>7/2</sub> spectra within the nano-particles regions are also in accord with that of the Rh 3d<sub>5/2</sub> spectra, indicating stronger Pt oxidation.

The relative depth of Rh and Pt oxidation in the particles can be elucidated from the attenuation of the metallic Rh and Pt components, using the classical photoelectron escape depth relationship and considering that the maximum probing depth under our experimental conditions is  $\sim 10$  Å. We estimated for the highest oxygen doses that at least three atomic layers of Rh atoms are oxidized ( $\sim 7-8$  Å), and in some regions (e.g. B) the extinction of the bulk component means that the oxidation depth exceeds 10 Å ( $\sim$ four layers). The Pt atoms are much more resistant to oxidation and the oxide formation is limited to the top two layers (3-4 Å). This means that the active catalytic state of the PtRh alloy catalyst under realistic oxidation-reduction conditions is characterized by very different Rh and Pt oxidation states at the surface and in the subsurface regions.

As explained in section 2.2.3 thanks to the multichannel electron detector it is possible to acquire within a single image several chemical maps and to extract spectra from some region inside the image.

The contrast of the Rh maps in Fig. 4.5 corresponds to the summed signal from all 48 channels covering the energy window of the Rh 3d<sub>5/2</sub> electron emission. As noted above, the absolute intensity is strongly affected by the topography artefacts, which can be removed using proper normalization procedures [2].

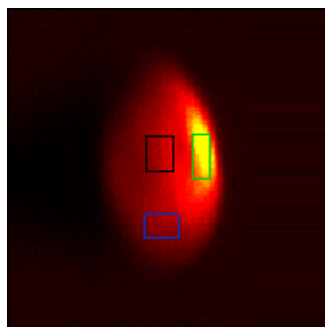


**Figure 4.5:** Rh 3d<sub>5/2</sub> 48-channels image. The colored squares indicate the regions within the particle where spectra were extracted and showed in Fig. 4.6.

Despite the intensity artefact the lineshape of the reconstructed spectra from different regions marked in Fig. 4.5 shown in Fig. 4.6 clearly evidences the spatial heterogeneity in the Rh oxidation state.

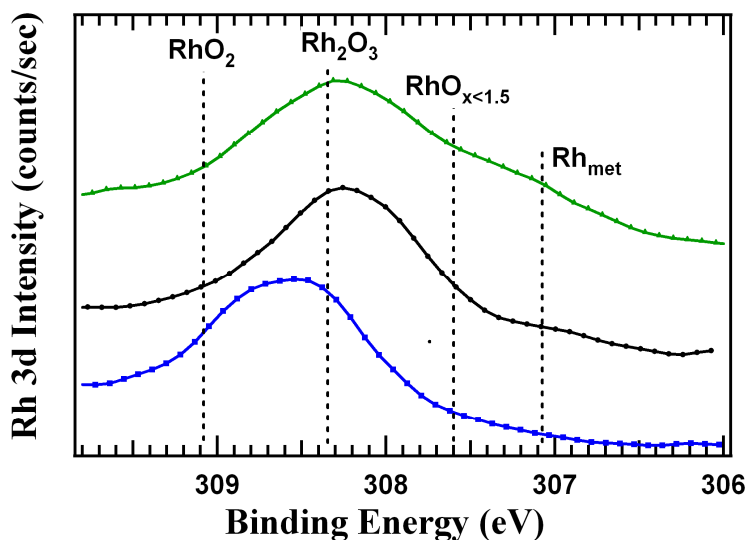


*Figure 4.6: reconstructed Rh 3d<sub>5/2</sub> spectra taken from the three different regions within the particle showed in Fig. 4.5. The differences in the local oxidation state are clearly manifested by the reconstructed spectra.*

The chemical maps, illustrating the spatial distribution of the different Rh oxidation states within the particle, are obtained by selecting channels covering the energy window of the corresponding components and dividing by the total 48-channel signal to remove the topography related artefacts.

The maps (Fig. 4.7) clearly show the coexistence of regions of different reactivity: it is possible to distinguish the weakly (top and right), moderate (middle) and strongly oxidized (bottom) regions where metallic Rh-RhO<sub>x</sub>, Rh<sub>2</sub>O<sub>3</sub> or RhO<sub>2</sub> state dominates. Note that the electron emission contributing to the metallic Rh signal comes from the atoms below the oxygen-containing top layers. The noisy region on the left side is the shadowed area, which impedes a reliable chemical analysis.

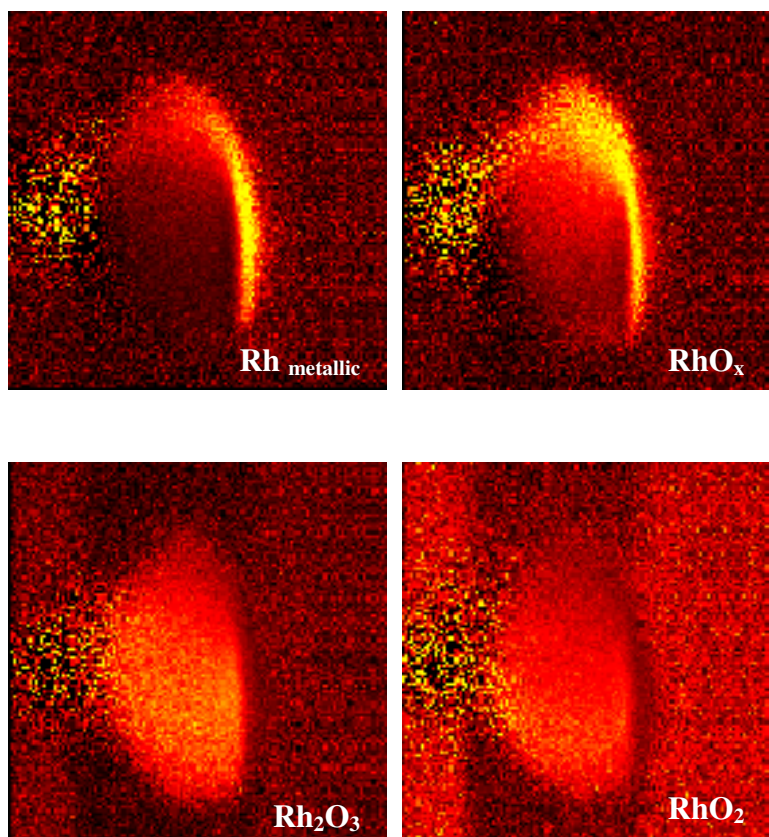


*Figure 4.7: Rh  $3d_{5/2}$  normalized chemical images of the  $RhO_2$ ,  $Rh_2O_3$ ,  $RhO_x$ , and  $Rh_{met}$  states. These images are generated by selecting the channels corresponding to a specific chemical state in the reconstructed spectra.*

The spatial heterogeneity of the Pt oxidation states is illustrated in Fig. 4.8.

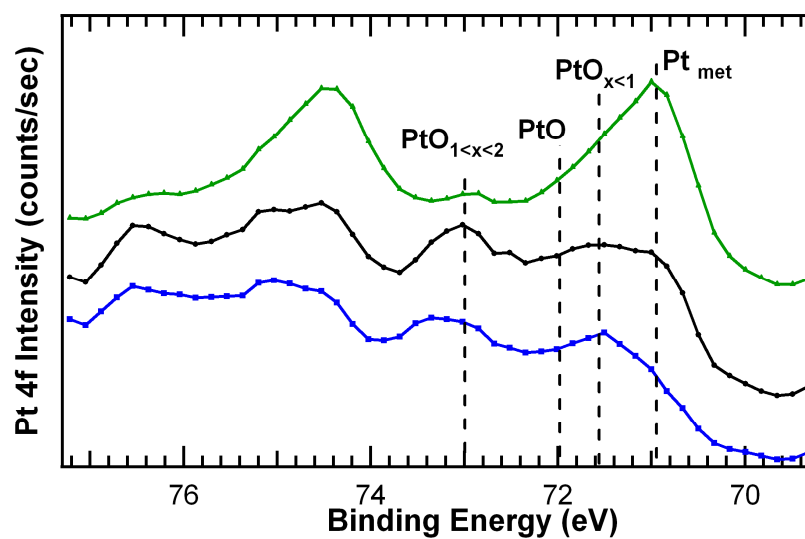


*Figure 4.8: reconstructed Pt  $4f_{7/2}$  spectra taken from the three different regions within the particle showed in Fig. 4.5. The differences in the local oxidation state are clearly manifested by the reconstructed spectra.*

Although measured with a lower energy resolution in order to cover the wider Pt  $4f_{7/2}$  energy range, one can clearly distinguish the main components, manifesting the differences in the oxidation state within the particle.

As for Rh the lateral distribution of each Pt phase is shown in Fig. 4.9. The right-hand border of the island is dominated by metallic and  $\text{PtO}_{x<1}$  states, replaced by  $\text{PtO}$  and  $\text{PtO}_{x>1}$  states, moving towards the central part. Comparison with the Rh chemical maps shows some correlations, e.g. both Rh and Pt appear in the lowest oxidation state in the top-right regions, which supposes that the local structure plays a dominant role. Only for the very bright stripe on the right-side edge, facing the grazing acceptance angle analyser, we cannot rule out that the enhanced emission from the Rh and Pt metallic atoms is not partially due to the local geometry, i.e. increased probing depth as a result of increased taking-off emission angle.

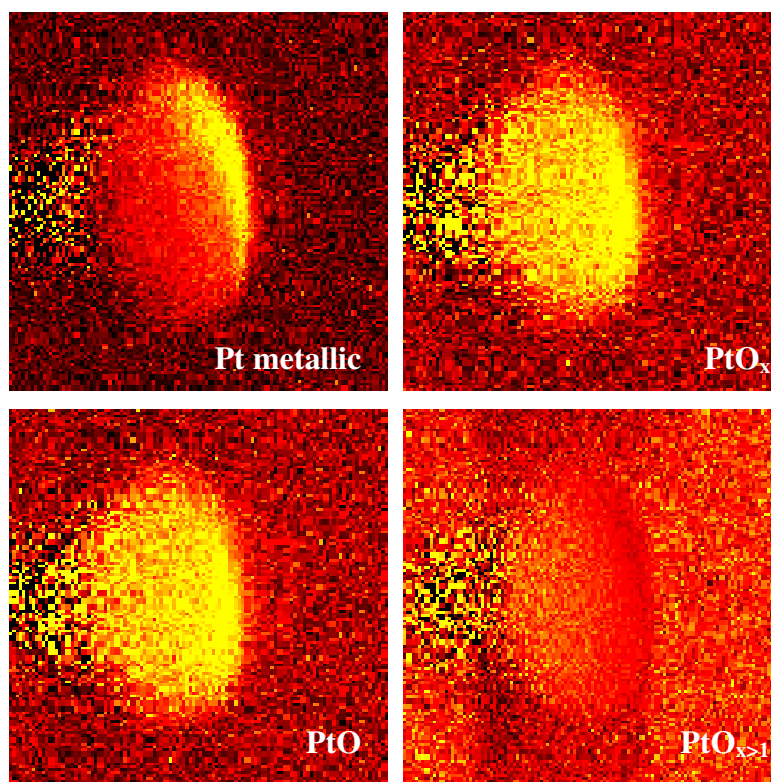


**Figure 4.9:**  $\text{Pt } 4f_{7/2}$  images of a PtRh micro-particle. The normalized  $\text{Pt } 4f_{7/2}$  chemical images are generated choosing the channels corresponding to a specific chemical states in the reconstructed spectra.

The relative weight of the oxidation states within the particle elucidated from the chemical maps is reported in Fig. 4.10.

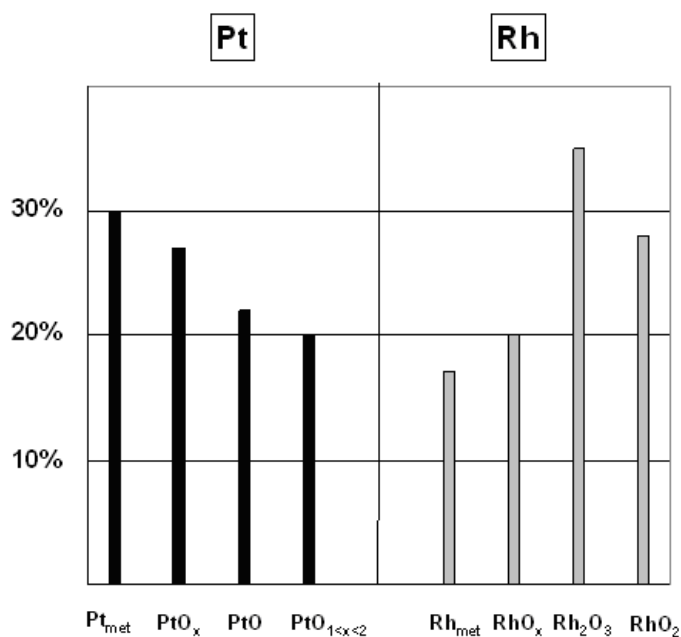


*Figure 4.10: Normalized distribution of the oxide phases on the PtRh particle evaluated by analyzing the data in Fig. 4.7 and Fig. 4.9.*

The metallic state corresponds to the sub-surface atoms and reflects only the thickness of the oxygen-containing top layers, which is apparently higher in the case of Rh. For Pt the lowest oxidation PtO<sub>x<1</sub> state is dominant, whereas Rh undergoes stronger oxidation and the Rh<sub>2</sub>O<sub>3</sub> dominates. It is quite clear from this plot that the top layers of the particles, which determine its reactive properties, contain coexisting Pt and Rh oxidation phases, which complicates the assignment of the reactivity to a single chemical state. One should consider that each phase presents at this complex chemically heterogeneous surface should have its local structure, which may play an important role for creation of active sites and/or accommodation of transition reaction states. We would like to notify that since the formed oxide phases have different stoichiometries and thicknesses, we cannot judge possible Pt-Rh ratio changes (Rh or Pt segregation) induced by the oxidation. As evidenced by the evolution of the surface structure under oxidation described in the next section the formed Pt and Rh oxide phases under our experimental conditions do not show any long-range order.

## References

- 1 Doniach, S.; Sunjic, M. *J. Phys. C* **1970**, 3, 285
- 2 Günther, S.; Kolmakov, A.; Kovac, J.; Kiskinova, M. *Ultramicroscopy* **1998**, 75 (1), 35-51
- 3 Baraldi, A.; Giacomello, D.; Rumiz, L.; Moretuzzo, M.; Lizzit, S.; Buatier De Mongeot, F.; Paolucci, G.; Kiskinova, M. *J. Am. Chem. Soc.* **2005**, 127, 5671-5674.
- 4 Mason, M.G. *Phys. Rev. B* **1983**, 27 (2), 748-762
- 5 Dudin, P.; Barinov, A.; Gregoratti, L.; Scaini, D.; He, Y.B.; Over, H.; Kiskinova, M. *J. Phys. Chem. C* **2008**, 112, 9040–9044.
- 6 Parkinson, C.R.; Walker, M.; McConville, C.F. *Surf. Sci.* **2003**, 545, 19-33
- 7 Yi-Chan, C.; Yu-Ming, S.; Shih-Ying, Y.; Chang-Po, H.; Jon-Yiew, G.; Chwung-Shan, K. *Nucl. Instr. And Meth. in Phys. Res. B* **2002**, 237, 296-300.

## Chapter 5

# Structural changes evidenced by LEEM and $\mu$ -LEED

For better understanding what happened to the particular structure of the clusters and to follow the changes occurred upon oxidation, we performed a number of oxidation and reduction treatments for 24 hours ending with a 2-hour long oxidation, monitoring the evolution and the transformation of the facets contrast with SEM images. The oxidation was made with the same plasma source, while the reduction was made by filling the chamber with molecular hydrogen at  $5 \times 10^{-6}$  mbar. In both case the sample was kept at 200°C.

Fig. 5.1 shows SEM images of two different PtRh clusters, in their reduced state after the deposition and after the redox treatment described above.

The contrast in the images has been enhanced in order to reveal all the changes occurred on the surface. The contrast of the particle in Fig.5.1a appears rather uniform, dominated by the donut-like morphology which generates artifacts in the picture. The same particle after the treatment, shown in Fig.5.1b, is more structured. Well separated regions with the same intensity are visible revealing the polycrystalline nature of the particle and their surface appears smooth. A different behavior is seen for the second particle. The map in Fig. 5.1c referred to the reduced state reveals a well defined structure of the surface; the boundaries between each grain/crystal appear sharp and the surface smooth. After the redox treatment and the final oxidation the main contrast between the grains is reduced but smaller agglomerates appears on the surface. It has to be remarked that this second behavior was observed in a limited number of particles, while for the majority the change in contrast/morphology resembles that of the first particle.

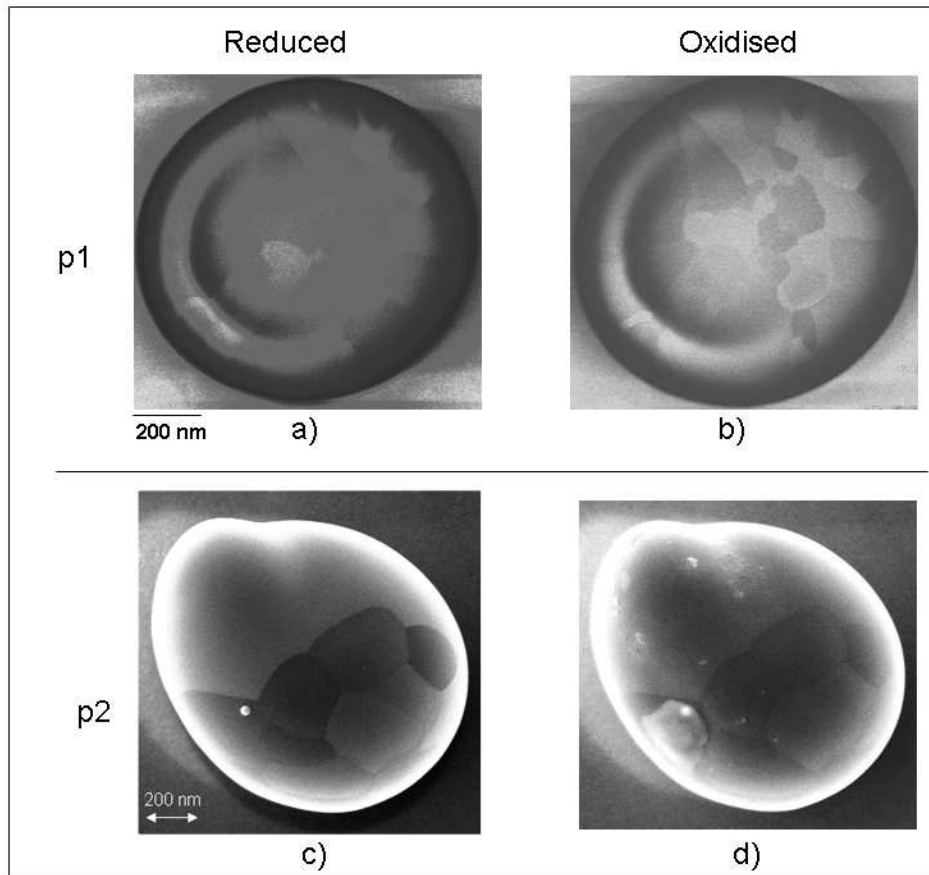


**Figure 5.1:** SEM images of two particles before and after 24 hours of a series of oxidation with atomic oxygen by plasma gun and further reduction with molecular hydrogen. The contrast of the facets with its orientation is enhanced.

Despite the SEM which is a mainly a morphological sensitive techniques and can provide limited information on the structure and the chemistry of the particles, the changes in the contrast suggested a dramatic transformation of their surface structure which deserves a more accurate analysis with complementary techniques. For this reason the particle alterations were monitored by LEEM and its  $\mu$ -LEED option which are surface structure sensitive technique able to fit our scale dimensions.

A  $\mu$ -LEED image of a cluster that cover the field of view of the instrument is shown in Fig. 5.2: the pattern is related to an entire single cluster where each spot is generated by a well oriented facet.

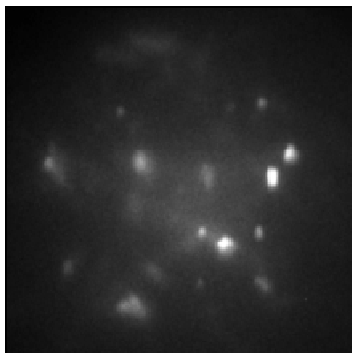


*Figure 5.2:  $\mu$ -LEED pattern related to an entire single particle where each spot is generated by a well oriented facet.*

If the primary diffracted beam (or “00” beam) is selected to perform imaging (LEEM Bright Field Imaging Mode) the resulting contrast in the maps is purely structural and depends on the local changes in the diffraction properties of the different surface phases present on the sample surface. The resulting image is shown in Fig. 5.3.

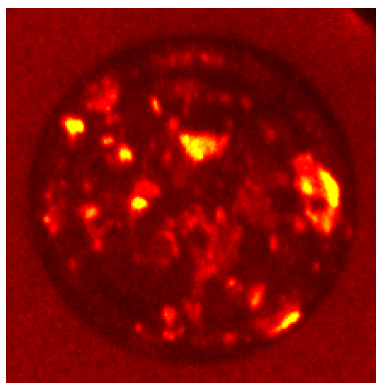


*Figure 5.3: Bright Field Image of a cluster. All the facets that correspond to a single spot of the LEED in Fig. 5.2 have been made visible together in the same image.*

If the secondary diffracted beam is selected (LEEM Dark Field Imaging Mode) than only areas that contribute to the formation of the selected beam appear bright. In Fig. 5.4 few dark field images are shown; in each one a single facet that corresponds to a specific spot energy in the  $\mu$ -LEED pattern and that reveals the different structures of several regions of the surface is visible.

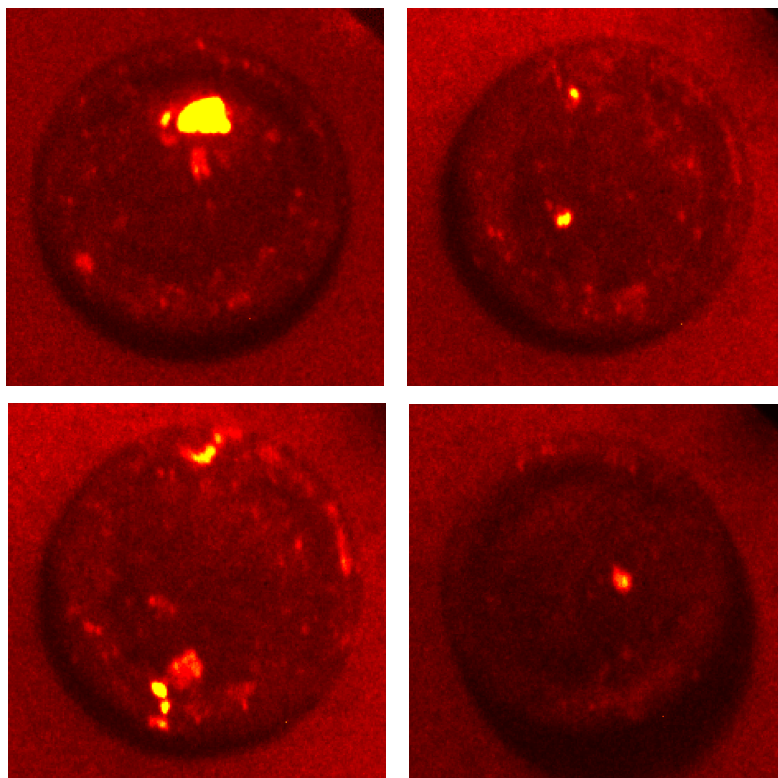


*Figure 5.4: Dark Field images taken at different spot energies revealing the different structures of several regions of the surface.*

A 2- $\mu\text{m}$  wide particle was selected for a LEEM and  $\mu$ -LEED investigation of the effects of the oxidation on the surface.

Prior to oxidation, the diffraction pattern (Fig. 5.5a) reveals the presence of several well-defined facets with different orientations with respect to the surface normal. This pattern reflects the existence of surface regions with a long range order, each producing well defined spots. The dark-field LEEM images displayed in Fig. 5.5b clearly show that each diffraction spot is identified with a nano-facet with sharp boundaries. Note that, in order to illuminate more than a single facet, many dark field images are superposed in Fig. 5.5b. Exposure to oxygen for 60' leads to deterioration of the LEED pattern and increasing the intensity of the diffuse background (see Fig. 5.5c). Nevertheless, some of the original spots can still be recognized, which suggests that the facets remain at least partially intact but with loss in the long range order. Indeed, superposition of dark field images in Fig. 5.5d shows the same facet boundaries, but the reduced contrast indicates different levels in structural deterioration between different facets. This confirms that the oxidation process proceeds differently on each facet in accordance with the observed spatial inhomogeneity in the oxidation states. Despite the differences in the lateral resolution of LEEM and SPEM measurements comparing the

SPEM results in figures. 4.7 and 4.9 (previous chapter) with the LEEM ones in Fig. 5.5, one can see that there is a good agreement between the SPEM chemical contrast and the structural LEEM contrast.

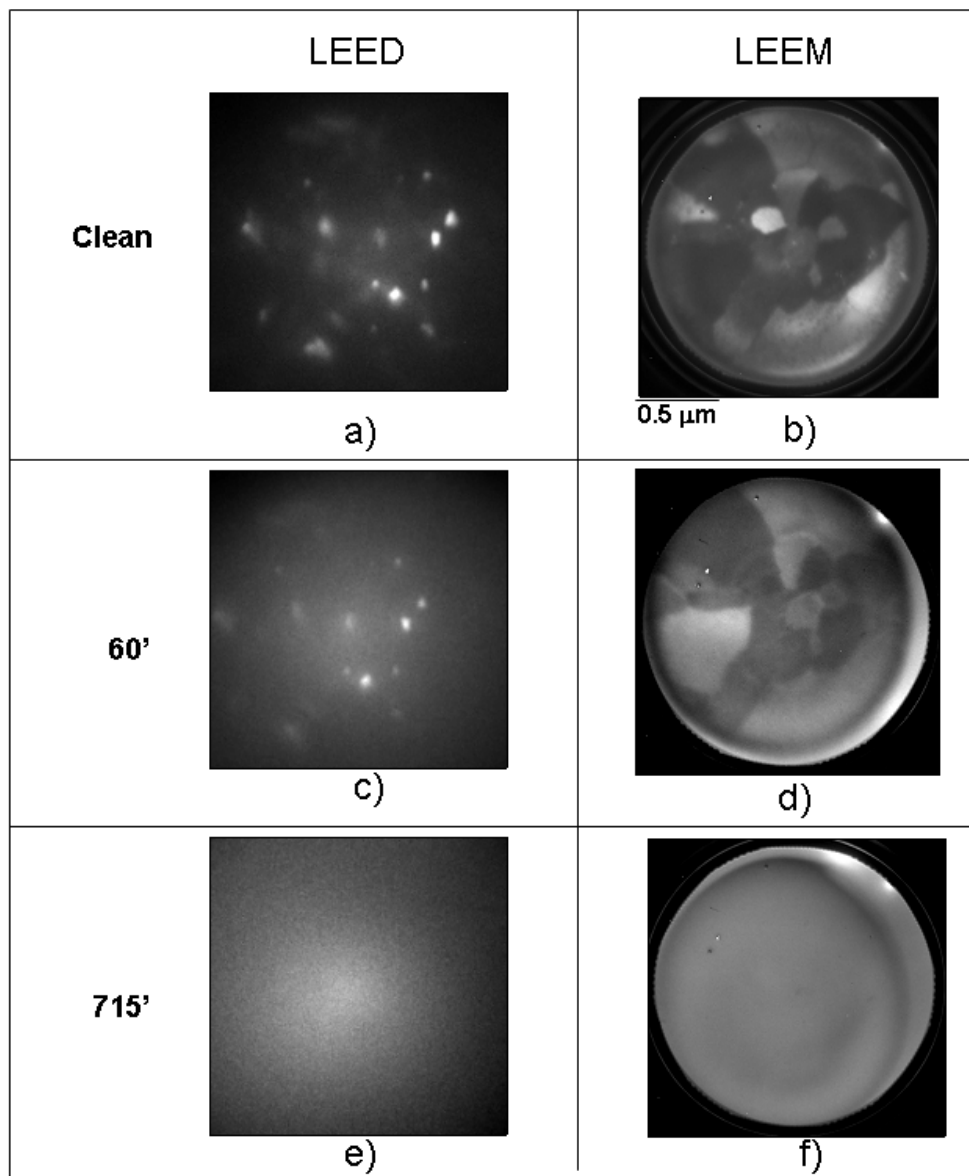


*Figure 5.5: (left) LEED patterns of a PtRh particle before and after a 60 and 715 min of oxygen exposures. Each diffraction spot is identified with a nano-facet in the corresponding dark-field LEEM images (right), where many dark field images are superposed in order to illuminate more than a single facet.*

This SPEM-LEEM correlation is a clear evidence that the oxidation rate is controlled by the local structure of the different facets, which is in accordance with the reported differences in the oxidation rate of differently oriented single crystal planes and the

'promotion' effect of structural irregularities [1]. More dramatic structural changes resulting in the extinction of LEED spots occur upon stronger oxidation. The LEED pattern from a heavily oxidized particle in Fig. 5.5e, shows only a strong diffuse background without any detectable diffraction spots. The loss of ordered atomic structure is confirmed by the corresponding LEEM image in Fig. 5.5f, which corresponds to an uniform disordered surface. According to the photoemission spectra in figures 4.6 and 4.8 this advanced oxidation state is characterised by rather thick O-rich Rh oxide phases while Pt undergoes milder oxidation, but the lateral variation in the oxidation state, i.e. the difference in the local reactivity is preserved. The fact that we still distinguish by SPEM coexistence of more than one Rh and Pt oxidation state within the regions appearing 'homogeneous' implies that these regions contain clusters with variable oxygen coordination of the Rh(Pt) atoms. These results are in general agreement with the structural alterations of supported Rh particles under oxidation conditions monitored by in-situ transmission electron microscopy and x-ray absorption spectroscopy [2, 3].

## References

---

- 1 Lundgren, E.; Mikkelsen, A.; Andersen, J.N.; Kresse, G.; Schmid, M.; Varga, P. *Journal of Physics Condensed Matter* **2006**, 18, R481-R499
- 2 Goller, H.; Penner, S.; Rupprechter, G.; Zimmermann, C. *Cat. Lett.* 2004, 92, 1, & Hannemann, S.; Grunwaldt, J.-D.; van Vegten, N.; Baiker, A.; Boye, P.; Schroer, C.G. *J. Phys. Chem. B* **2006**, 110, 8674
- 3 Hannemann, S.; Grunwaldt, J.-D.; van Vegten, N.; Baiker, A.; Boye, P.; Schroer, C.G. *J. Phys. Chem. B* **2006**, 110, 8674

# Chapter 6

## Other results

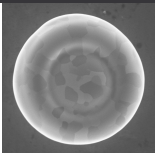
### 6.1. Bulk-surface stoichiometry

The chemical composition of the surface as the termination of  $\text{Pt}_x\text{Rh}_y$  oriented single crystals has been object of intense investigation in last two decades. Most of the experimental and theoretical simulations performed on Pt-Rh alloys with different bulk stoichiometry have demonstrated the general trend of a Pt enrichment of the termination layers. Despite the evidence that this is the main tendency suggested by energetic and thermodynamic considerations, the segregation behaviour can be significantly altered by kinetic limitations and other factors such as the annealing at high temperatures, the presence of adsorbates (e.g. sulphur) or the reaction with hydrogen [1, 2, 3]. Despite the large number of studies on single crystals, no reference has been found which concerns the investigation of the stoichiometry of PtRh clusters or deposited films produced by any technique. For this reason the data reported in this section can be considered as the first indication of the PLD effects on the chemical composition of the particles produced.

#### 6.1.1. PE and EDX measurements

PLD is becoming a diffuse technique for the production of thin films of metals. For instance the possibility to realize the cathodes of the fuel cells by PLD is deeply delved. On the other hand, the physical and chemical processes which occur during the PLD process are extremely complex and can strongly modify the local chemistry of the sampled irradiated. The extremely fast annealing time due to the enormous heat transfer

produced by the short laser pulse and the fast quench of the cluster after their landing on the surface generate a process far from any equilibrium process. In order to evaluate the effects of these processes on the elemental composition of the PtRh clusters photoemission and EDX measurements have been performed and compared. The probing depth of the two techniques mentioned was  $\sim 1$  nm and  $\sim 2$   $\mu\text{m}$  respectively making possible to compare surface and bulk compositions. As reference the Pt<sub>50</sub>Rh<sub>50</sub> target has been measured first.

		Surface (PE)	Bulk (EDX)
<b>Pt<sub>50</sub>Rh<sub>50</sub> Target</b>		Pt rich At % (Rh-Pt)= 41-59	Pt = Rh At % (Rh-Pt)= 50-50
<b>PLD Cluster</b>		Rh rich At % (Rh-Pt)= 79-21	Rh rich At % (Rh-Pt) = 52-48
<b>Flat</b>		Rh rich At % (Rh-Pt)= 58-42	//

*Table 6.1: results of the different chemical composition of the PtRh alloy in the Pt<sub>50</sub>Rh<sub>50</sub> target and in the clusters produced by PLD (nano and micro size) measured in photoemission and in fluorescence.*

The results, reported in the Table 6.1, show a perfect agreement of the compositions of the target with the nominal values for the EDX measurements and a Pt enrichment of the surface of about 9% as shown by the PE measurements. A significant change in the composition occurs when the clusters are measured. A large number of clusters with diameters ranging from 200 to 2000 nm have been probed in order to provide a sufficiently large statistics. The PE quantifications show a large increase of the Rh content on the surface of the clusters which strongly attenuates in the bulk where the values are very close to the target ones. The change in the chemical composition of the clusters is related to their size; the PE measurements performed on the regions covered with nanosized islands, in fact, still show an increase of the Rh content but much lower

than the larger clusters. Due to the low coverage of the nanosized cluster it was not possible to detect any EDX signal from the related Pt and Rh atoms.

The results obtained unambiguously state a strong dependence of the chemical composition of the termination layers of the clusters from their size. Cause the spatial resolution of the SPEM it was not possible to perform a systematic probe of the stoichiometry between the macro and nanoscopic particles, i.e. to determine if the Pt surface content linearly decreases with the downsizing of the clusters or if a threshold dimension exists.

## **6.2. Morphological changes by annealing**

The oxidation and reduction of the PtRh particles was mainly performed while keeping the sample at 200 °C. This temperature was selected in order to increase the kinetics of the redox processes without affecting too much other phenomena such as the mass transport (induced also by the gas phase reactions) or the desorption of the adsorbed gases. Nevertheless it turned out to be interesting to understand what happened to the particles when exposed to higher temperatures which could be necessary for several catalytic reactions. Due to the limited time available only the SEM investigation of the effects of the temperature on the particles has been performed. Nevertheless the evolution of the morphology of the particles has revealed unexpected results.

### **6.2.1. Evolution of the morphology analyzed by SEM**

Fig. 6.1 shows one of the PtRh particle selected to probe the temperature effects. This image corresponds to the particle imaged right after its deposition at room temperature. As reported in the previous chapters the typical donut-like shape and oriented facets are well visible.

The sample has been annealed at four different temperatures (400°C, 500°C, 650°C and 850 °C) each kept for 30 minutes. The annealing has been performed in a UHV ambient with a background pressure of  $\sim 1 \times 10^{-8}$  mbar. After each treatment the sample was removed from the UHV chamber and inserted in the SEM chamber for the characterization. This step included an exposure of the sample to the ambient pressure which certainly oxidised the surface.

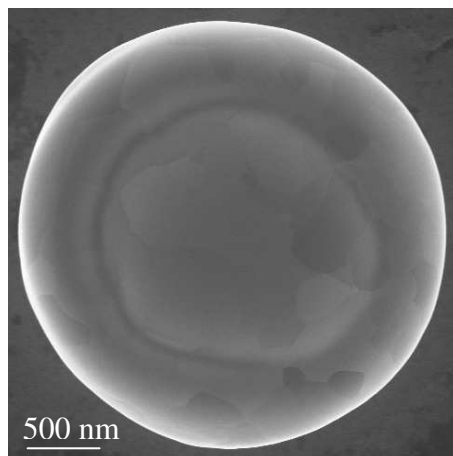


**Figure 6.1:** SEM image of one cluster deposited by PLD at room temperature before starting the annealing process.

The effects of the temperature on the particle shown in Fig. 6.1 have been reported in Fig. 6.2.

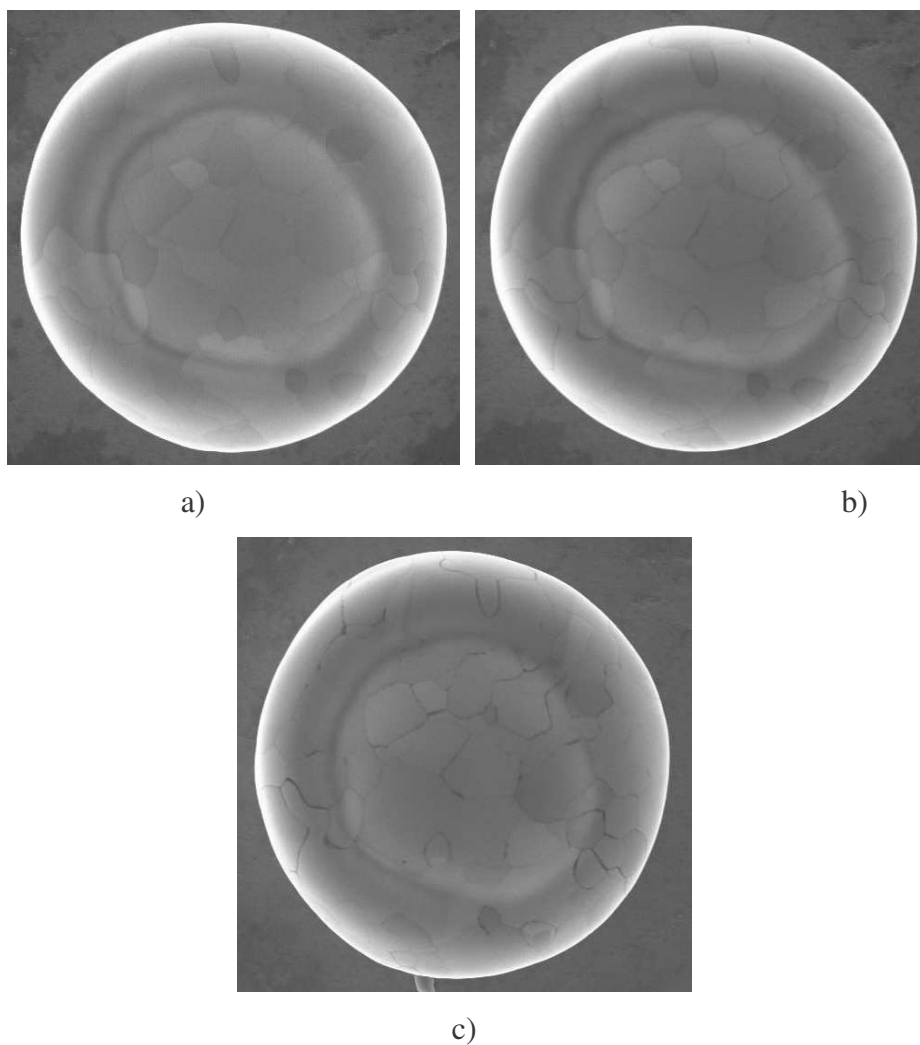


**Figure 6.2:** SEM images of the same cluster after three different annealing temperatures. a) 400°C, b) 500°C and c) 650°C.

After the annealing at 400 °C (Fig. 6.2a) the contrast between the grains appearing on the surface is more pronounced. Since the sample has been exposed to air prior to the SEM image, we can not exclude that this change is just due to the oxidation of the surface. More evident mutations of the surface have been recorded after the annealing at 500 °C and 650 °C. Fig. 6.2b and Fig. 6.2c showing the particle after these two temperatures, in fact, clearly indicate an increase of the separation between each grain composing the particle. Boundaries become deeper resembling a canyon-like shape. This is even more evident in the high resolution maps shown in Fig. 6.3 and 6.4. In spite of the clear tendency of the boundaries between the grains to become larger and deeper it is not possible from these images to evaluate to which extent the separation of the grains occurs while moving inside the particle.

Moreover the top grain visible in Fig. 6.3 seems partially collapsed i.e. at a lower level with respect to the surrounding regions.

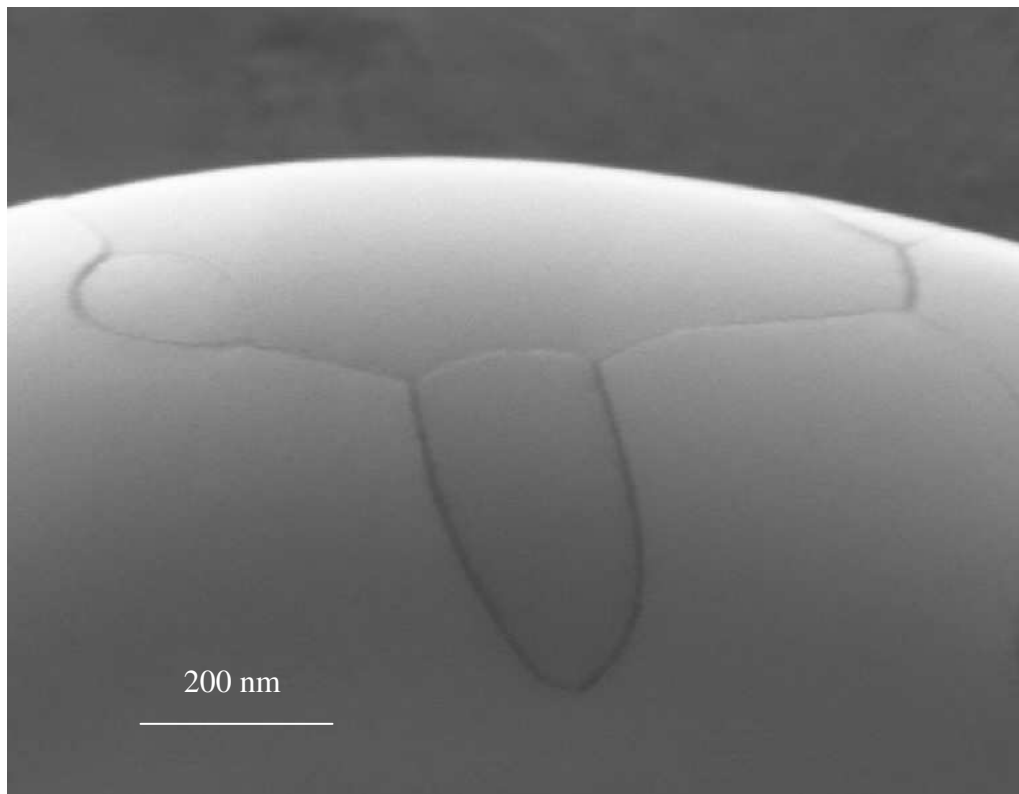


**Figure 6.3:** high magnification SEM image that shows the collapsing of one facet respect the surrounding others.

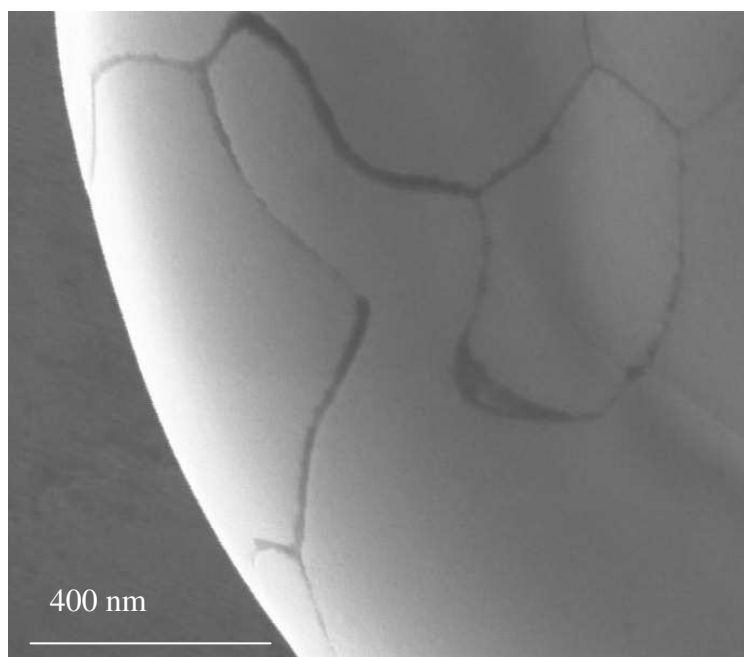


**Figure 6.4:** high magnification SEM image that shows in particular what happens between the boundaries of the facets.

A dramatic change has been observed after the annealing at 850 °C; the image in Fig. 6.5 shows the particle which appears melted in the outer part while the old structured

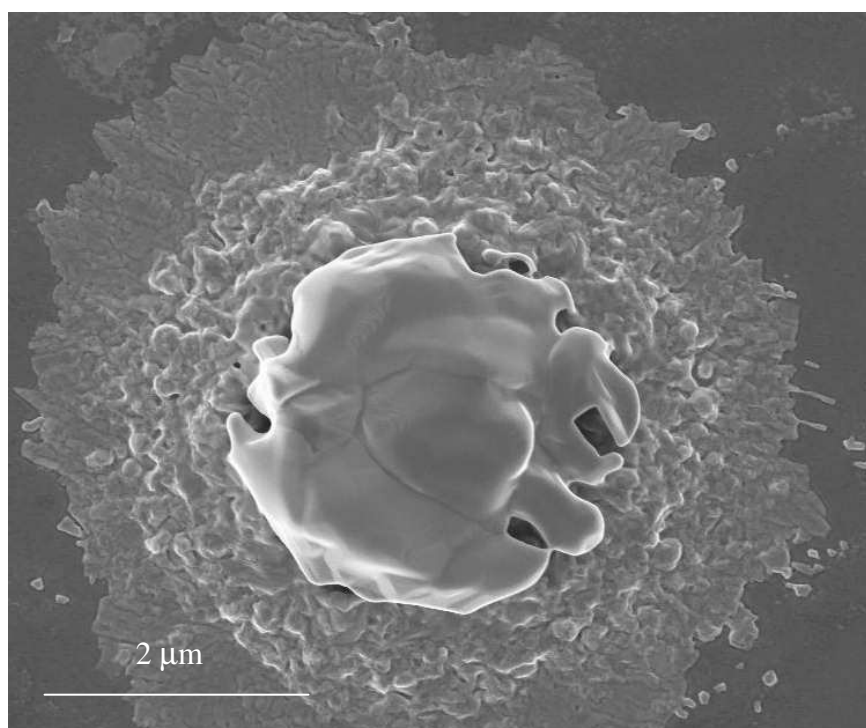


**Figure 6.5:** SEM image of the cluster after annealing at 850°C. The outer part of the cluster is melted and the previous structure exist only in the centre parte.

morphology is still present only in the centre. It is worth to note that the region covered by the melted part is larger than the original size of the particle. The original grainy structure of the particle is completely vanished in the melted region which now appears formed by small agglomerates; also the central area appears strongly modified.

The Pt-Rh phase diagrams found in the literature do not show any eutectic point which decreases the melting point to such low temperatures. In Fig. 6.6 a phase diagram calculated from theoretical calculation found in ref. [4] is shown; at the alloy concentration used for our experiments the melting point is well below the temperature scale reported in the graph.

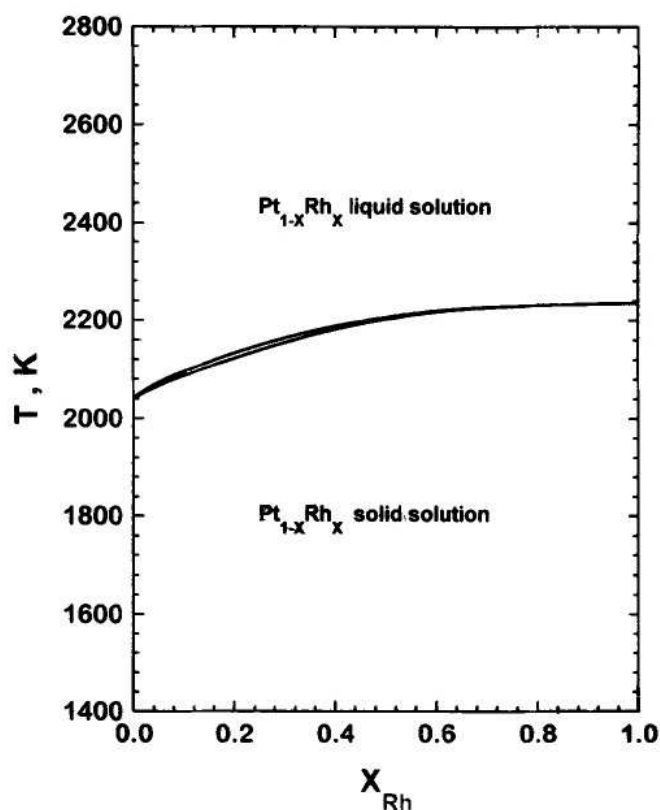


*Figure 6.6: phase diagram for the system Pt-Rh (Jacob et al. 1998)*

The experimental observation of an extremely low melting temperature must be related to the technique used for the production of the clusters (PLD). Moreover it must be noted that from our characterization approach the internal structure of the particles is completely unknown. The presence of oxide phases inside the particle (and on the surface since before each SEM characterization the sample was exposed to air) could also destabilise the structure as suggested in ref. [4].

### 6.2.2. Stoichiometry after annealing

After the annealing process at 850 °C, EDX measurements have been performed in order to establish if some stoichiometric changes occurred inside the compact part of the particle and outside of it in the melted region. A sufficiently large number of particles have been probed in order to identify a common trend in the change of the stoichiometry.

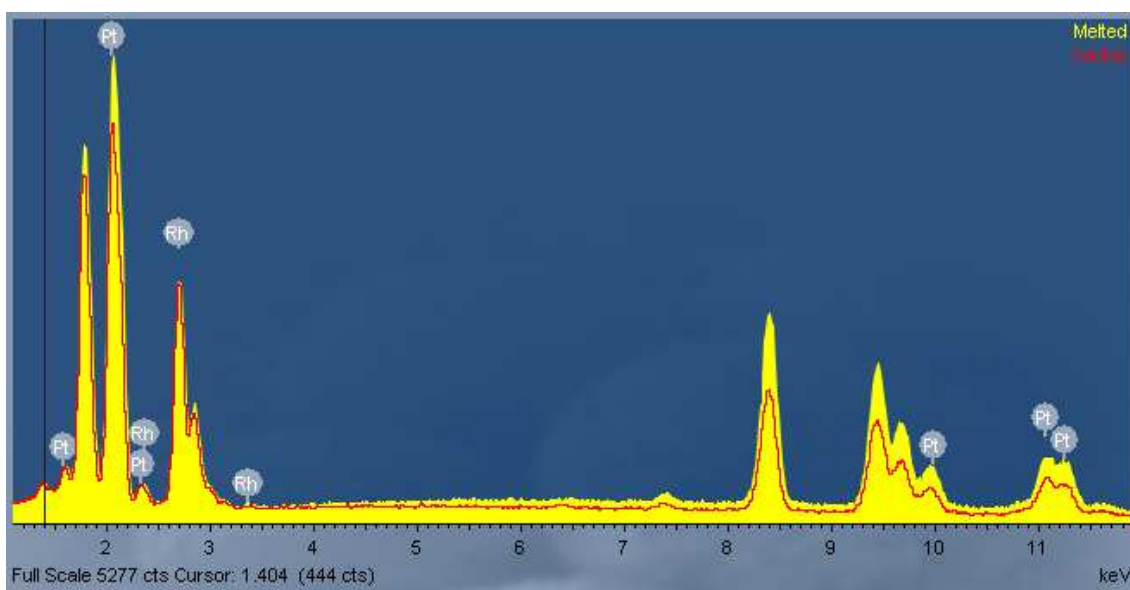


**Figure 6.7:** EDX spectra taken at the centre of a melted PtRh (red) and outside the particle (yellow) in the melted part. The two spectra intensities are normalized with respect to the Rh  $L\alpha_1$  at 2.69 keV.

Fig. 6.7 report two EDX spectra taken on a particle similar to those reported in Fig. 6.5: the two spectra are collected in the melted part of the particle (bold-yellow) and in the central part (red) and their intensities have been normalized with respect to the Rh  $L\alpha_1$  line at 2.69 keV. The change in the chemical composition of the two parts is clear. While the melted regions maintains the same stoichiometric ratio between Pt and Rh present before the annealing (as can be seen by comparing the EDX spectrum of Fig. 2.18 with the yellow one of Fig. 6.7), the central area shows a drop of the Pt content of about 40%. In other words the central region now becomes Rh-rich. This behaviour has been observed in all the melted particles.

### 6.3. Photon Beam Induced Reduction

It is well known that the extremely intense focused beam of the SPEM ( $10^{18}$  photons/( $\text{mm}^2 \text{ s}$ )) can produce undesired artefacts generated by the interactions of a large number of photons with the matter. In the reference [5] the main effects have been reported in detail.

Reduction of oxide samples is one of the most commonly observed photo-chemical processes [6]. The loss of oxygen, first reported for high valence metal oxides, is driven by inter-atomic Auger de-excitation after creation of a core hole in the metal ion, which leads to ejection of  $\text{O}^+$  ions [7]. Various oxide surfaces can be subjected to photo-reduction; for example organic samples, simple metal oxides, such as  $\text{TiO}_2$ , Mo oxides,  $\text{WO}_3$ ,  $\text{CeO}_2$  [8] and complex oxide systems as  $\text{SrTiO}_3$ , bismuthates, etc. [9] have shown the tendency to reduce after irradiation. The long experience of the SPEM team in measuring different materials has shown that for the transition metal oxides the irradiation resistance depends on the actual stoichiometry and the long-range structural order of the regions irradiated. Disordered oxide phases and thin oxide films with not well-established structure are usually more vulnerable. As a side effect of the phenomena in some cases the reduction of the surface could be used to monitor the stability of the surface phases and can provide important information.

#### 6.3.1. Ageing effects after redox cycles

In the PtRh system a significant photon induced reduction of the oxide phase has been observed after a procedure aimed to simulate an ageing effect of the particles itself. The spectra displayed in Fig. 6.8a and Fig. 6.9a show the effect of the focused beam on the surface of a micron-sized particles oxidised by 765 min of plasma source.

Three successive spectra for the Rh 3d and two following spectra for the Pt 4f show a weak effect of the beam which tends to reduce the surface. The differences in the shape of the spectra for the Rh core level are negligible while for the Pt a more pronounced effect is observed. Afterwards the particle has been exposed to a 48 hours long redox procedures where time-variable oxidations under atomic oxygen at 200 °C and reductions with molecular hydrogen ( $P = 5 \cdot 10^{-6}$  mbar) at the same temperature cycles

have been performed. After the same final oxidation of 765 min, the same particle has been measured.

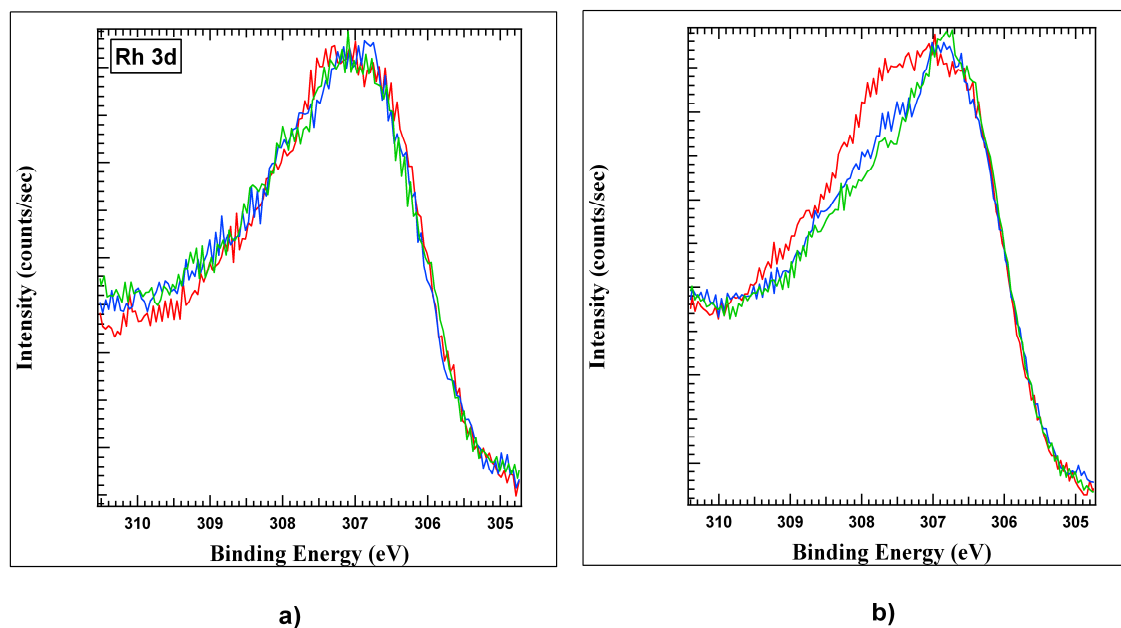


*Figure 6.8: a) Rh3d<sub>5/2</sub> spectra taken on a micron-sized cluster after 765 min of oxidation, and b) after 48 hours of redox cycles and a same final oxidation.*

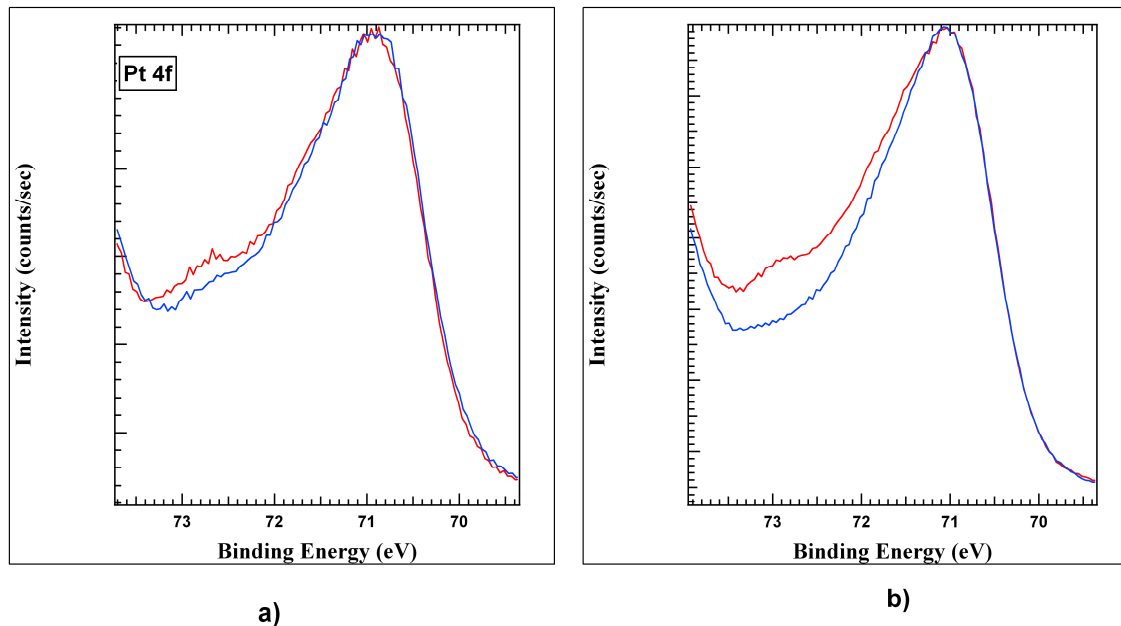


*Figure 6.9: a) Pt4f<sub>7/2</sub> spectra taken on a micron-sized cluster after 765 min of oxidation, and b) after 48 hours of redox cycles and a same final oxidation*

The resulting evolution of the spectra is reported in Fig. 6.8b for the Rh 3d and in Fig. 6.9b for the Pt 4f. A clear change in the reduction rate of both elements is visible. As introduced above this evidence should indicate a dramatic change in the structural order

of the oxide phases formed after the “ageing” process applied to the particles. The data available do not allow a clear correlation between the stoichiometry of the oxide phases as measured by photoemission before and after the “ageing” which appears similar (the oxidation condition was in fact the same for both cases). It is preferable at this step just to show the bare effect of the reduction that to try a speculative analysis following the fit of the spectra.

## 6.4. Partial coverage of a single multi-wall carbon nanotube

### 6.4.1. Carbon Nanotubes (CNTs)

Carbon nanotubes (CNTs) [10] are unique nanosystems with extraordinary mechanical and electronic properties, which derive from their unusual molecular structure. An ideal carbon nanotube can be thought of as a single graphite layer (graphene sheet), rolled up to make a seamless hollow cylinder (Fig. 6.10). These cylinders can be tens of microns long, with diameters as small as 0.7 nanometres and are closed at both ends by fullerene-like caps. CNTs having wall thickness of one carbon sheet are named single-wall carbon nanotubes (SWCNTs). In consequence of the van der Waals interactions between nanotubes, they often aggregate in large ropes. SWCNTs can be considered as the building blocks of multi-wall carbon nanotubes (MWCNTs), which consist of a coaxial array of SWCNTs with increasing diameter. MWCNTs are also usually long

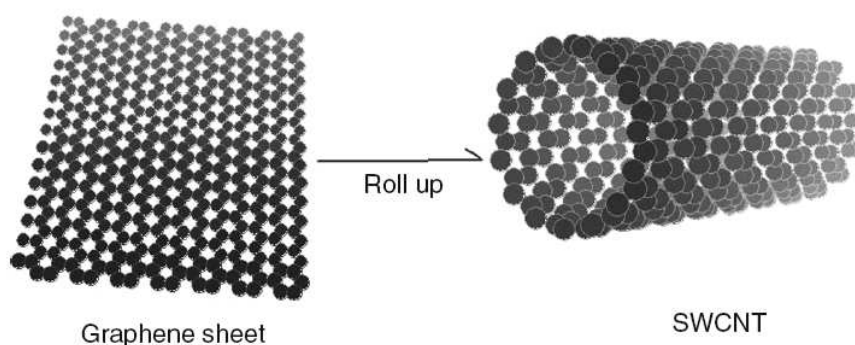


*Figure 6.10: rolling up of a grapheme sheet to make a SWCNT*

several microns, with the external diameter that ranges from two to several tens of nanometres, providing very high aspect ratio structures. MWCNTs consist of more than

one carbon nanotube arranged concentrically around the axis of the inner tube and having increasing diameters and different helicities.

The outer diameter of MWCNTs depends on the technique used to grow them; multi-wall carbon nanotubes either with diameter of a few nanometres and bigger than 100 nanometres can be produced.

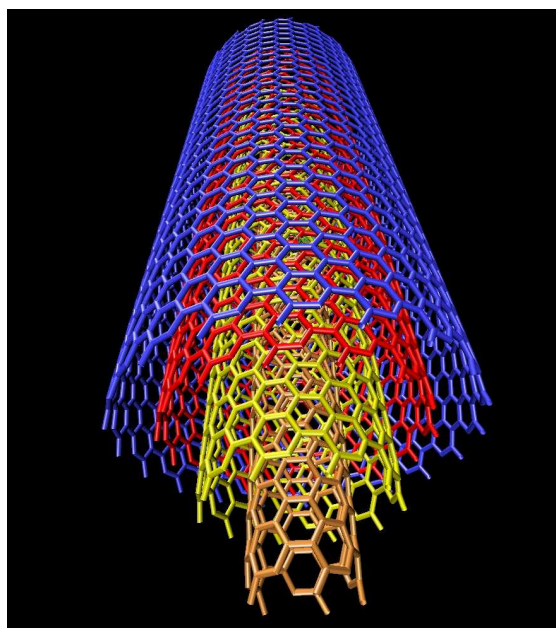


*Figure 6.11: structure of a multi-walled nanotube.*

Many potential applications have been proposed for carbon nanotubes, including conductive and high-strength composites; energy storage and energy conversion devices; sensors; field emission displays and radiation sources; hydrogen storage media; and nanometer-sized semiconductor devices, probes, and interconnects. In addition CNTs are potentially excellent supports for other materials such as functionalized coatings or nanostructured catalysts. Their morphological, mechanical, chemical and electronic properties, in fact, make them suitable for many applications. In this section the attempts to achieve a partial coverage of a single MWCNT are reported. A confined patch of metallic coating on a CNT, for instance, opens the possibility for the SPEM for a detail investigation of phenomena such as the mass transport, the surface and bulk diffusion, etc.

### 6.4.2. Experimental setups for the partial coverage of a single MWCNT

In Fig. 6.12 SEM images of high density ( $10^9 \text{ cm}^{-2}$ ) and low density ( $10^6 \text{ cm}^{-2}$ ) aligned multiwall carbon nanotubes arrays are shown. This configuration of CNTs is ideal for SPEM experiments. The best lateral resolution achievable in imaging mode ( $<50 \text{ nm}$ ) allows the investigation of the CNT from their side, i.e. in a cross sectional view. In this way the entire length of a single CNT with diameter down to  $50 \text{ nm}$  can be analysed. The density of the array should not exceed a critical number if the goal is to identify isolated CNT far apart each other.

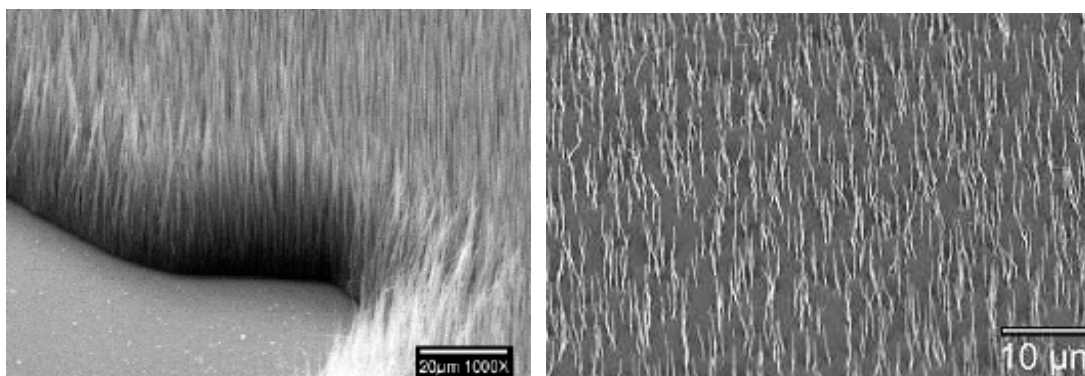


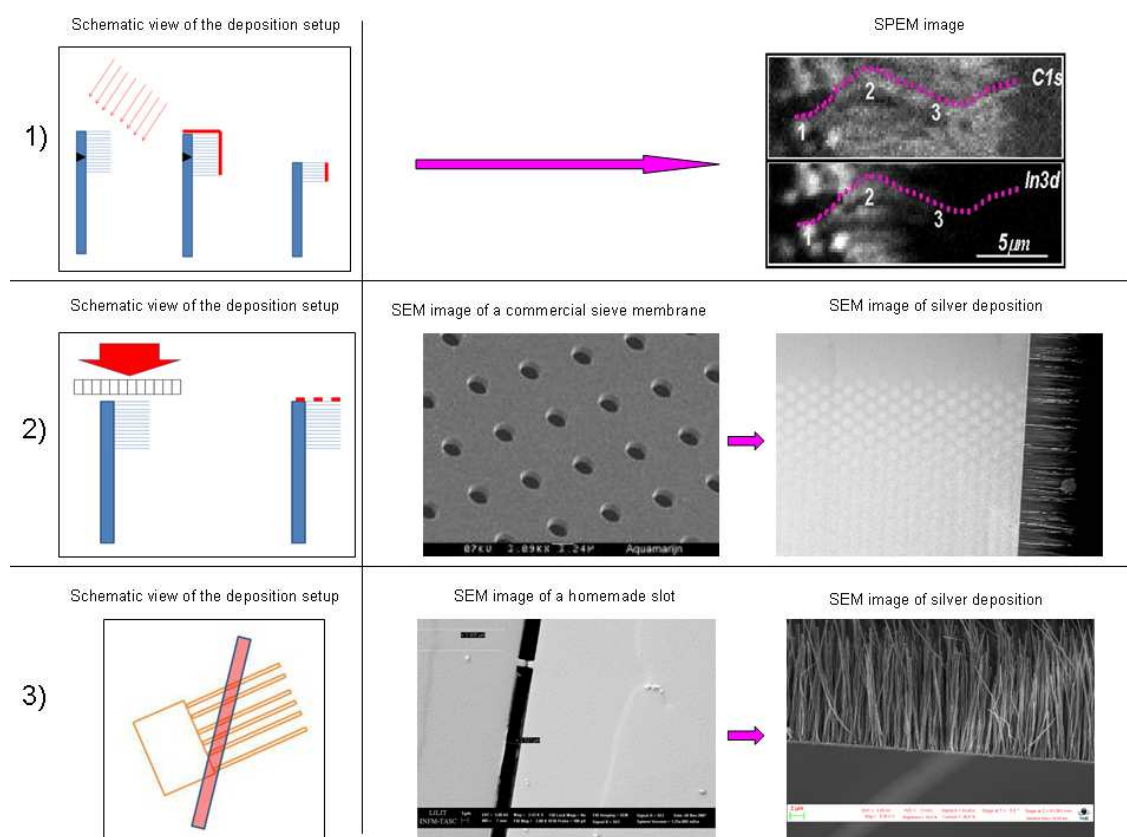
**Figure 6.12:** high density ( $10^9 \text{ cm}^{-2}$ ) and low density ( $10^6 \text{ cm}^{-2}$ ) aligned carbon nanotubes arrays. For the high density array the nanotube length is  $1\text{-}20 \mu\text{m}$  and the diameter is  $30\text{-}150 \text{ nm}$ , in the case of low density array the length is  $1\text{-}5 \mu\text{m}$  and diameter is  $50\text{-}150 \text{ nm}$ .

Different approaches have been followed in order to achieve the result of a partial coverage (for instance the evaporation of a metal) of a single CNT. Fig. 6.13 summarizes the attempts and results obtained; the first method consists of a grazing deposition of a metal on the array as shown in the figure. The sample is then cleaved leaving just the tips of the CNT covered. This approach works well only for highly dense arrays which results, as visible in the figure, in chaotic SPEM images where it is difficult to identify a single CNT. Another disadvantage is that the central part of the CNT remains clean.

The second approach is based on the use of masks with a large number of small holes. Masks of this type are available commercially but they do not match the ideal parameters in terms of hole size and hole to hole spacing. It is possible to produce ideal

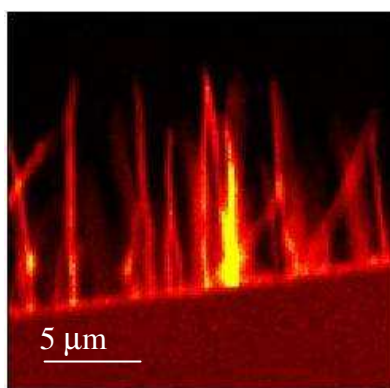
masks following lithographical techniques, but for extended areas the resulting supports are very fragile.

The best results have been obtained by using home made very narrow slits from metallic rigid fenditures. With the use of well-known mask alignment techniques it is possible to realize slits 1-3  $\mu\text{m}$  wide and 1-2 mm long which are not commercially available. As visible in the SEM picture of Fig. 6.13, different regions of the MWCNT side wall can be covered.



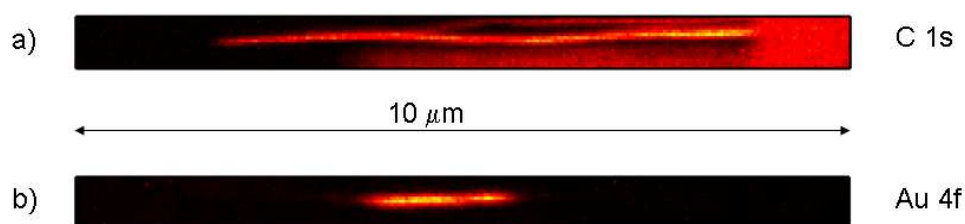
**Figure 6.13:** different approaches for a partial of a single CNT 1) The first method consists of a grazing deposition of a metal on the array. The sample is then cleaved leaving just the tips of the CNT covered. The SPEM image on the right shows the result of this deposition. 2) The second approach is based on the use of available commercially masks (like sieve membrane) with a large number of small holes. SEM image on the right show the deposition in correspondence of the holes. 3) The third method uses a home made very narrow slits from metallic rigid fenditures done with lithographical techniques. With the use of well-known mask alignment techniques it is possible to realize slits 1-3  $\mu\text{m}$  wide and 1-2 mm like in the SEM image on the right.

Fig. 6.14 shows a SPEM picture of a low density array of MWCNTs. Individual MWCNT with width down to 50 nm can be identified and measured.



**Figure 6.14:** SPEM image taken at the C 1s energy of a low density CNTs sample perpendicular to the support substrate.

An example of partial coverage of a single CNT is reported in Fig. 6.15. A 2- $\mu\text{m}$  Au patch has been deposited on the central part of a CNT as shown by the C 1s and Au 4f maps



**Figure 6.15:** a) carbon image of a single entire CNT; b) gold image of the same wire: the gold was evaporated only in the middle part of the CNT using a mask like the one described above.

Due to the time limitation imposed by this thesis work only preliminary experiments dealing with the PLD deposition of PtRh particles on confined regions of MWCNT have been performed. They have been shortly summarised in the next section.

### 6.4.3. Deposition of PtRh clusters on MWCNTs

The deposition of the PtRh particle on the MWCNT arrays has been performed by following the same procedures and parameters described in the previous chapters. Nevertheless the different geometrical setup of the sample holder needed to accommodate the arrays in their cross-sectional view has modified the density of the particles deposited. Fig. 6.16 shows two SEM pictures of MWCNTs covered by few

PtRh particles. Image a) shows a 50 nm large particle attached to the tip of the MWCNT while image b) reveals the presence of few nanometre scale particles close to a larger one attached along the MWCNT side.

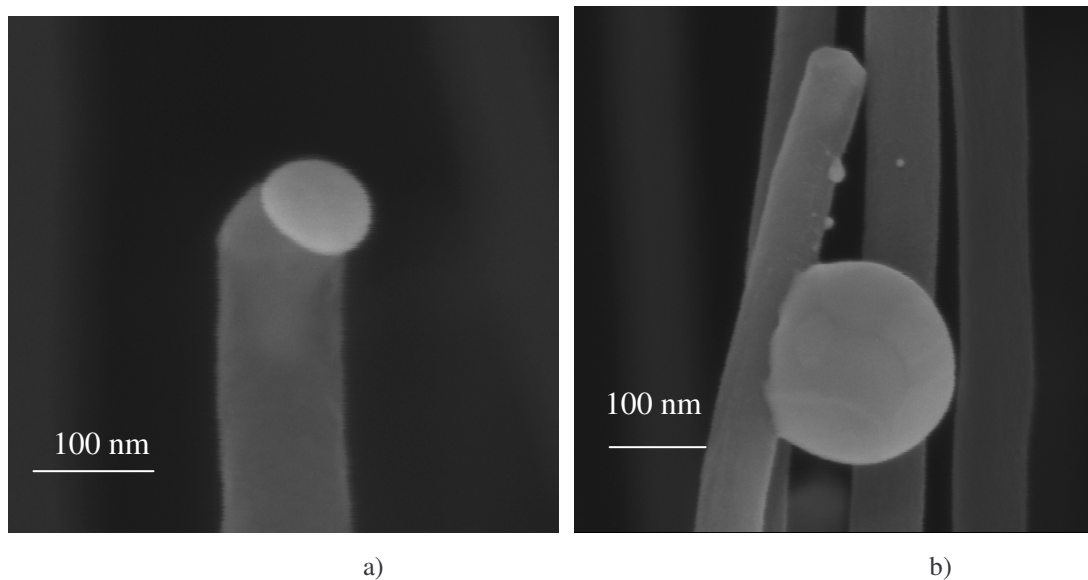


*Figure 6.16: SEM images of nano-sized PtRh clusters deposited on single MWCNT.*

Regions where a higher density of particles is present have been found as visible in Fig. 6.17; due to the particular morphology of MWCNTs a very high resolution microscopy like TEM would be necessary to identify and investigate the smaller clusters in the nanometre range.

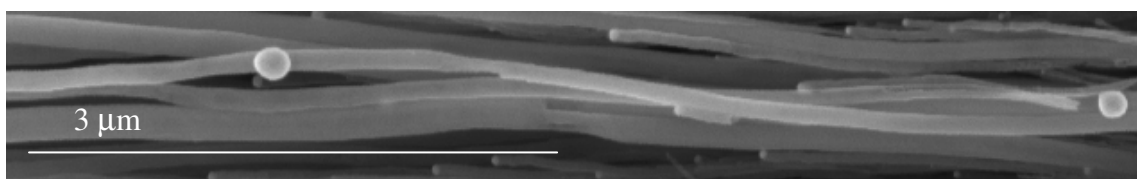


*Figure 6.17: two PtRh clusters deposited on a single MWCNT: one at the bottom and one in the middle of the wire.*

---

**References**

---

- 1 Wouda, P.T.; Nieuwenhuys, B.E.; Schmid, M.; Varga, P. *Surface Science* **1996**, 359, 17-22.
- 2 Baraldi, A.; Giacomello, D.; Rumiz, L.; Moretuzzo, M.; Lizzit, S.; Buatier De Mongeot, F.; Paolucci, G.; Kiskinova, M. *J. Am. Chem. Soc.* **2005**, 127, 5671-5674.
- 3 Zhu, L.; Wang, R.; King, T.S.; DePristo, A. E. *Journ of Catalysis* **1997**, 167, 408-411.
- 4 Jacob, K.T.; Priya, S.; Waseda, Y. *Bull. Mater. Sci.* **1998**, 21, 99-103.
- 5 Gregoratti, L.; Mentès, T.O.; Locatelli, A.; Kiskinova, M. *Journal of Electron Spectroscopy and Related Phenomena* **2009**, 170, 13–18.
- 6 Ramsier, R.D.; Yates, J.T. *Surf. Sci. Rep.* **1991**, 12, 243, and the references therein.
- 7 Feibelman, P.J.; Knotek, M.L. *Phys. Rev. B* **1978**, 18, 6531.
- 8 Locatelli, A.; Pabisiak, T.; Pavlovska, A.; Mentès, T.O.; Aballe, L.; Kiejna, A.; Bauer, E. *J. Phys.: Condens. Matter* **2007**, 19, 082202.
- 9 Zakharov, A.A.; Johansson, U.; Leandersson, M.; Nylén, H.; Ovarford, M.; Lindau I.; Nyholm, R. *Phys. Rev.* **1997**, B56, 5755.
- 10 Iijima, S. *Nature* **1991**, 354, 56.

# Chapter 7

## Conclusions

In spite of the progress made, monitoring the local chemical state of a single catalyst particle and providing a strict morphology control remain unresolved problems even during preparation of model catalysts. Apart from instrumental limitations to control the morphology, in fact, there are many reasons that prevent the particles to attain the predicted equilibrium shape, such as strain at the interface, temperature-induced reduction in surface energy anisotropy, coalescence during the growth process, etc. In the case of alloy systems, the complications due to uncertainty regarding metal particle size, morphology and structure are further exacerbated by added ambiguities concerning the particle surface composition.

In the present thesis work using a combination of chemical imaging, micro-spectroscopic and structural methods with sub-micron spatial resolution, we explored the oxidation of supported PtRh micro- and nano- particles to derive structure-reactivity and size-reactivity relationships. The most important findings, which are a step towards bridging the material gap in catalyst research, are listed below.

1. Independently of the particle size Rh oxidises faster than Pt and a thick Rh oxide layer is formed in the advanced oxidation state. Both  $\text{Rh}_2\text{O}_3$  and  $\text{RhO}_2$  stoichiometric phases form and coexist in the advanced oxidation stage, whereas the oxidation of Pt is limited only to the top few layers without reaching the highest  $\text{PtO}_2$  oxidation phase. In accordance with previous studies for oxidation of PtRh alloys, the evolution of the Pt 4f and Rh 3d spectra are identical to those reported during oxidation of Pt and Rh alone, i.e. the two metals preserve their relative reactivity and there is no indication for formation of a mixed oxide phase.

2. The Pt and Rh degrees of oxidation showed marked lateral variations within a single micro-particle. This inhomogeneity in the oxidation states correlates to the initial complex surface structure of the micro-particles consisting of facets with different orientations and degree of surface order, which determines the local oxidation rate.
3. The oxidation process is accompanied by continuous structural changes and loss of the ordered atomic structure on the facets. The most advanced oxidation state is characterised with a disordered surface, concomitant with the observed coexistence and random distribution of many oxidation phases consisting of clusters where Rh and Pt have reached different degrees of oxidation.
4. The size-effect is clearly manifested by the higher Pt and Rh oxidation states of the nano-particles compared to the micro-particles under identical reaction conditions. However, the more advanced oxidation state attained by the nano-particles cannot be considered as a simple size effect, since it is obscured by uncertainty regarding their morphology and structure.

In summary, our findings demonstrate that determining and controlling the particles morphology, structure and composition and their evolution under reaction conditions is of the utmost importance. The present results show that changes may occur on very local microscopic scales resulting in structural and compositional heterogeneity. The observed compositional complexity of the PtRh particles and the loss of a long range order under oxidation conditions support the most recent views that the catalytically active states under operation conditions are not well-defined and ordered stoichiometric phases but are dynamic states lying often at the boundary between two phases. This also suggests that in catalytic reactions only fractions of the particle surface can behave as an active catalyst, i.e. looking for simple size-activity trends on assumption of a known equilibrium shape, structure and composition is far from the reality. It is the challenge of the years to come to gain detailed structural knowledge with careful chemical analysis probing single nano-particles.

Other results have shown that the stoichiometry of the PtRh particles produced by PLD depends on their size and is different from values reported in the literature for PtRh

alloy bulk crystals. PLD seems to affect also other parameters such as the phase diagram of this compound which seems to be present a low melting point. All these findings that have been only partially addressed stimulate the research on this topic; additional experiments have been already scheduled to shed light on these and other aspects still unclear.

# List of publications

Dudin, P., Barinov, A., Dalmiglio, M., Gregoratti, L., Kiskinova, M., Goriachko, A., Over, H., “*Nanoscale morphology and oxidation of ion-sputtered Rh(110) and Ru(0001)*”, 2008 Journal of Electron Spectroscopy and Related Phenomena 166-167 (1-3 C), pp. 89-93.

Bhuvana, T., Gregoratti, L., Heun, S., Dalmiglio, M., Kulkarni, G.U., “*Electron resist behavior of pd hexadecanethiolate examined using x-ray photoelectron spectroscopy with nanometric lateral resolution*”, 2009 Langmuir 25 (2), pp. 1259-1264.

Barinov, A., Malcioğlu, O.B., Fabris, S., Sun, T., Gregoratti, L., Dalmiglio, M., Kiskinova, M., “*Initial stages of oxidation on graphitic surfaces: Photoemission study and density functional theory calculations*”, 2009 Journal of Physical Chemistry C 113 (21), pp. 9009-9013.

Bozzini, B., Dalmiglio, M., De Gaudenzi, G.P., D'Urzo, L., Gregoratti, L., “*An investigation of the corrosion of WC-Co cermets in CN--containing aqueous solutions*”. Part II: Synchrotron-based high lateral-resolution XPS study, 2009 Corrosion Science 51 (8), pp. 1675-1678.

Dalmiglio, M., Amati, M., Gregoratti, L., Menteş, T.O., Niño, M.A., Felisari, L., Kiskinova, M., “*Oxidation of supported PtRh particles: size and morphology effects*”, Journal of Physical Chemistry C, accepted.

# Acknowledgments

*First of all, I would like to thank all the former and present colleagues and friends who helped me during these years and for the very intense and fruitful team work. I am very grateful to dr. Luca Gregoratti for giving me the opportunity to work in the ESCAMicroscopy group and for his support and help throughout my research. In fact I accepted to stay here in Trieste and to obtain a PhD title because of his kindness, humanity and friendliness. It's not so easy to find people you can work so serenely with and that who give you understanding and support in a way that allows you to wake up every morning and go to work with happiness.*

*Moreover I'm very grateful to all the other people that helped me with their presence, friendship and competence. In particular I would like to thank the following persons: Alexei Barinov, Matteo Amati, Majid Kazemian Abyaneh and Maya Kiskinova of the ESCAMicroscopy group, Andrea Locatelli, Teyfik Onur Menten, Miguel Angel Nino Orti of the Nanospectroscopy group, Laura Felisari for the hundreds of SEM images, Denis Scaini and Pietro Parisse for the AFM measurements, Mauro Prasciolu for the lithographic works, Annalisa Boscaino and Giusy Palma for all the time we spent together in the canteen and at the coffee machine, and all the other colleagues that I met at Elettra.*

*Last but not least I want to thank all my friends in Trieste for their liking, kindness and support: these three years flew away very fast thanks to all the good time that I spent with them. And of course I would like to thank my parents who sustained me with comprehension, affection and nearness although I was far from them.*